International Journal of Nanomedicine

Dovepress
open access to scientific and medical research

Open Access Full Text Article

ORIGINAL RESEARCH

Dual Stimuli-Responsive Micelles for Imaging-Guided Mitochondrion-Targeted Photothermal/ Photodynamic/Chemo Combination Therapy-Induced Immunogenic Cell Death

Yan Liang[1,2], Ping-Yu Wang[1], Ze-Yun Liu[3], Hong-Fang Sun[1], Qin Wang[1], Guang-Bin Sun[1], Xia Zhang[1], You-Jie Li[1], Shu-Yang Xie[1,2]

[1]Department of Biochemistry and Molecular Biology, Binzhou Medical University, YanTai, ShanDong, 264003, People's Republic of China; [2]Department of Physiology and Pathophysiology, School of Basic Medicine, Qingdao University, QingDao, ShanDong, 266071, People's Republic of China; [3]School of International Studies, Binzhou Medical University, YanTai, ShanDong, 264003, People's Republic of China

Correspondence: Shu-Yang Xie; You-Jie Li, Department of Biochemistry and Molecular Biology, Binzhou Medical University, YanTai, ShanDong, 264003, People's Republic of China, Tel/Fax +86 535 6913166; Tel/Fax +86 535 6913335, Email shuyangxie@aliyun.com; youjie1979@163.com

Introduction: As the special modality of cell death, immunogenic cell death (ICD) could activate immune response. Phototherapy in combination with chemotherapy (CT) is a particularly efficient tumor ICD inducing method that could overcome the defects of monotherapies.

Methods: In this study, new dual stimuli-responsive micelles were designed and prepared for imaging-guided mitochondrion-targeted photothermal/photodynamic/CT combination therapy through inducing ICD. A dual-sensitive methoxy-polyethylene glycol-SS-poly (L-γ-glutamylglutamine)-SS-IR780 (mPEG-SS-PGG-SS-IR780) polymer was synthesized by grafting IR780 with biodegradable di-carboxyl PGG as the backbone, and mPEG-SS-PGG-SS-IR780/paclitaxel micelles (mPEG-SS-PGG-SS-IR780/PTXL MCs) were synthesized by encapsulating PTXL in the hydrophobic core.

Results: In-vivo and -vitro results demonstrated that the three-mode combination micelles inhibited tumor growth and enhanced the therapeutic efficacy of immunotherapy. The dual stimuli-responsive mPEG-SS-PGG-SS-IR780/PTXL MCs were able to facilitate tumor cell endocytosis of nanoparticles. They were also capable of promoting micelles disintegration and accelerating PTXL release. The mPEG-SS-PGG-SS-IR780/PTXL MCs induced mitochondrial dysfunction by directly targeting the mitochondria, considering the thermo- and reactive oxygen species (ROS) sensitivity of the mitochondria. Furthermore, the mPEG-SS-PGG-SS-IR780/PTXL MCs could play the diagnostic and therapeutic roles via imaging capabilities.

Conclusion: In summary, this study formulated a high-efficiency nanoscale platform with great potential in combined therapy for tumors through ICD.

Keywords: immunogenic cell death, photothermal/photodynamic/chemo therapy, dual-stimuli-responsive, poly(amino acid)s micelles, imaging-guided therapy, mitochondria targeting

Introduction

Immunogenic cell death (ICD) is distinctive modality of cell death, with high immunogenicity that is able to elicit tumor cell immune response.[1–3] Cancer-occurring ICD provides damage-associated molecular patterns (DAMPs) and tumor-associated antigens to increase the immunogenicity of cancer cells.[4–6] Currently, the hallmark DAMPs comprise calreticulin (CRT), high-mobility group protein B-1 (HMGB-1), and adenosine triphosphate (ATP).[7,8] These immunogenic substances trigger dendritic cell maturation and promote T cell activation, proliferation, and differentiation to enhance antitumor autoimmunity.[9,10] Studies indicated that some chemotherapeutics, such as paclitaxel (PTXL), could cause ICD. However, a single agent is still difficult to achieve the ideal antitumor effect. In clinic, to sufficiently induce potent ICD, high drug doses are required. Serious toxic side effects and multidrug resistance (MDR) phenomenon make it difficult to achieve.[11,12] Various inducers or drug combination have

Received: 13 March 2023
Accepted: 14 July 2023
Published: 2 August 2023

potential to enhance the induction efficiency and immunologic effect of ICD, activate distinct signaling pathways, reduce drug resistance, and improve drug safety.[13] Aside from chemotherapy (CT), phototherapy and ionizing radiation are capable of inducing ICD.[14–16]

Among various types of phototherapy agents, IR780 iodide (IR780), a hydrophobic heptamethine cyanine dye, is considered to have clinical application value due to the dual-modality photothermal (PTT) and photodynamic (PDT) therapy, its capacity of mitochondrion targeting, excellent NIR fluorescence ability, and high aqueous stability.[17,18] IR780 also acts as a potent inducer of ICD and triggers T cell-provoked antitumorigenic immunity.[19,20] IR780 combined with PTXL not only increases the therapeutic effect but also minimizes the toxic side effects to overcome the disadvantages of monotherapy. However, because of the short half-life in circulation, poor stability, and inconsistent bio-distribution and pharmacokinetics, the application of combinational therapy in-vivo is limited. An intelligent tumor microenvironment (TME)-responsive nano-drug delivery system, which could efficiently combine IR780 with PTXL to take the synergistic effect and achieve a significant breakthrough in limited ICD treatment effect, is urgently needed.[21]

Poly(amino acid)s (PAAs) are formed by the polymerization of amino-acid building blocks. The abundant side active groups, easy fabrication and functionalization, and excellent biocompatibility and biodegradability on PAAs offer incomparable advantages in the nanomedicine field.[22] Polyethylene glycol (PEG)-PAAs are a representative class of nanocarrier drug-delivery systems, and multiple antitumor-drug carriers have already moved to clinical phases. For example, the carrier material of micelle-encapsulated doxorubicin formulation (NK911), which has entered Phase II clinical trials, is a PEG-poly(aspartic acid) diblock copolymer; the carrier material of docetaxel micelle (NK105), which has entered Phase III clinical trials, is a PEG-poly (aspartic acid) diblock copolymer; and the carrier material of cisplatin-incorporated polymeric micelle (NC-6004), which has entered phase III clinical trials, is a PEG-poly(glutamic acid) diblock copolymer.[23,24] Previous studies have designed and synthesized poly(L-γ-glutamylglutamine)-PTXL (PGG-PTXL) conjugates, which are formed by grafting glutamic acids to poly(L-γ-glutamic acid) and then conjugating PTXL.[25,26] Compared with the mono-carboxyl group on poly(L-γ-glutamic acid) chain, di-carboxyl group provides sufficient load-bearing capability for the grafts and offers the flexibility for spontaneous self-assemble into polymeric micelles. PGG-PTXL could improve the solubility of PTXL, and preclinical studies have confirmed its safety and effectiveness.[27,28]

The intra-tumor environment is different from blood circulation and normal tissues. The tumor intracellular glutathione (GSH) is >10 mM, which is well above the extracellular environment of 20–40 μM.[29,30] Meanwhile, the tumor intracellular pH (4.0–6.5) is below extracellular 7.4.[31–33] The dual stimuli-responsive and imaging-guided amphiphilic polymer methoxy-polyethylene glycol-SS-poly(L-γ-glutamylglutamine)-SS-IR780 (mPEG-SS-PGG-SS-IR780) was designed in accordance with the above triggered responses inside the tumor cells. In contrast to some direct IR780-loading nanoparticles, IR780 grafting could obtain high loading rate and stability while effectively dealing with thermal damage to the surrounding tissue. IR780 efficiently colocalizes with nanoparticles in in-vivo imaging, thus guaranteeing true monitoring without pre-leakage.[34–36] Furthermore, mPEG coated on the surface of nanoparticles could prevent rapid clearance by the reticuloendothelial system (RES) and achieve favorable long-circulation in-vivo.[37,38] After reaching the tumor site, dual stimuli-responsive bonds rupture and facilitate tumor cell endocytosis of nanoparticles.[39,40]

In this study, through a series of chemical reactions, an imaging-guided mitochondrion-targeted amphipathic polymer-IR780 conjugate (mPEG-SS-PGG-SS-IR780) was designed as a nano-vehicle, and PTXL was encapsulated into polymer micelles by self-assembly. This study proposed the hypothesis that once the micelles (mPEG-SS-PGG-SS-IR780/PTXL MCs) received intravenous administration, the long-circulation nanoparticle could passively target and accumulate in tumors on the basis of enhanced permeability and retention (EPR) effect. Under special TME, the cleavage of pH-sensitive amide bond and reduction-sensitive disulfide bond, which are linked with PEG, could result in dePEGylation and facilitate cellular internalization. After the internalizing process was achieved by tumor cells, nanoparticles tended to target the mitochondria, causing them to dysfunction. As photosensitizers upon NIR light irradiation, mPEG-SS-PGG-SS-IR780/PTXL MCs demonstrated PTT and PDT and killed cancer cells. Coupled with dual-stimuli responsiveness and PTT triggering the collapse of micelles, the rapid PTXL release achieved multi-modality PTT/PDT/CT synergistic tumor therapy and simultaneously induced tumor ICD. Given that the mitochondria are sensitive to hyperthermia and reactive oxygen species (ROS), the mitochondrion-targeted mPEG-SS-PGG-SS-IR780/PTXL MCs made mitochondrial function impaired easily.[41] The heat generated by near Infrared (NIR) also improved cell membrane permeability and enhanced cellular uptake. With the aid of imaging capability, diagnosis and treatment were

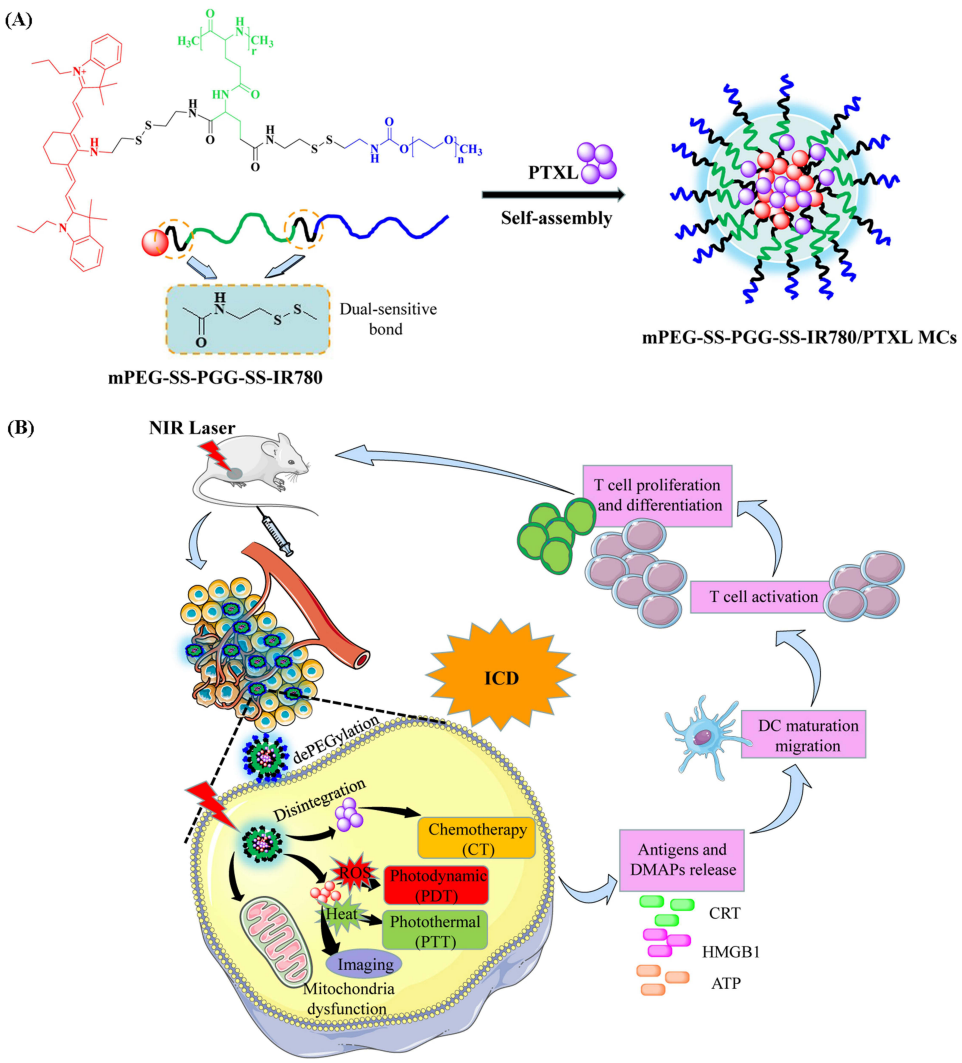

Scheme 1 Schematic (**A**) and intracellular performance (**B**) of mPEG-SS-PGG-SS-IR780/PTXL MCs.

integrated after single administration of mPEG-SS-PGG-SS-IR780/PTXL MCs (Scheme 1). The results revealed that mPEG-SS-PGG-SS-IR780/PTXL MCs significantly enhanced the efficacy of immunotherapy and obviously inhibited tumor growth. Therefore, these dual stimuli-responsive nanomicelles may be used as novel drug carriers for tumor-targeted therapy through multimodal synergistic therapy and ICD induction under the guidance of NIR fluorescence imaging.

Materials and Methods

Materials

H-Glu(OtBu)-OtBu·HCl and 1-hydroxybenzotriazole (HOBt) were purchased from J&K Chemical (China). 4-nitrophenyl chloroformate (NPC), triphosgene, cystamine dihydrochloride, γ-benzyl-L-glutamate, 1-ethyl-3-(3-dimethyl aminopropyl) carbodiimide hydrochloride (EDC·HCl), 4-dimethylaminopyr idine (DMAP), and pyrene were purchased from Aladdin (Shanghai, China) and used as received. N,N'-dimethylformamide (DMF) and trimethylamine (TEA) were dried and filtered before use. Hoechst 33,342 and 3-(4,5-dimethylthiazol-2-yl)-2,5-diphenyltetrazolium bromide (MTT) were purchased from Sigma-Aldrich (USA). Bovine serum albumin, RPMI-1640 medium, and trypsin-EDTA were obtained from Hyclone (USA). 2′,7′-Dichlorofluorescin diacetate (DCFH-DA) was obtained from Beyotime Institute of Biotechnology (Nantong, China). PTXL injections were supplied by Beijing Union Pharmaceutical Factory (Beijing, China). Alcohol, sodium methoxide, hydrochloric acid, and other chemicals were obtained from local commercial suppliers.

Synthesis of mPEG-SS-PGG-SS-IR780

The detailed synthesis steps of mPEG-SS-PGG-SS-IR780 conjugates are described in Figure 1.

Synthesis of mPEG-SS-NH_2

NPC (12.1 mg) and TEA (10.4 μL) were added dropwise to anhydrous DMF containing 95 mg of mPEG under stirring. After 3 h, the mixture was refluxed. The obtained product was concentrated and precipitated in cold methyl alcohol. Finally, NPC-active copolymer was dried under vacuum.

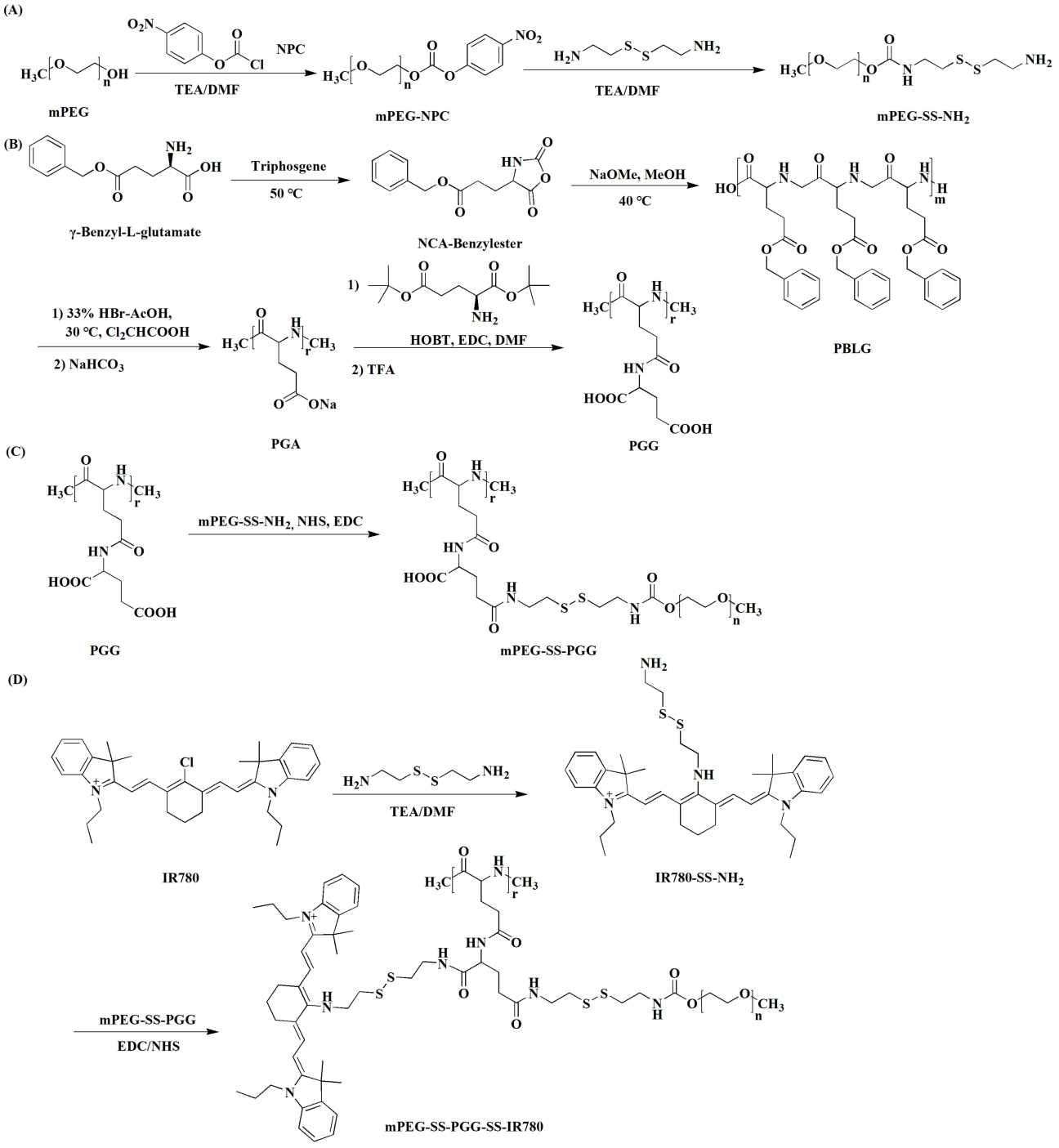

Figure 1 Synthesis routes of mPEG-SS-PGG-SS-IR780 conjugates (via steps (**A**–**D**)).

Cystamine dihydrochloride (22.5 mg) and TEA (28 μL) were dissolved in DMF at 0 °C. Then, 2 mL of anhydrous DMF solution of 40 mg mPEG-NPC was added dropwise under stirring. After 48 h, the mixture solution was recrystallized from cold ether. The final powder was obtained after vacuum drying, and ^{1}H-NMR spectra were recorded.

Synthesis of PGG

γ-Benzyl-L-glutamate (100 mg) was dissolved in 4 mL THF at 50 °C. After the solution was stirred for 5 min in nitrogen environment, THF solution containing 48 mg of triphosgene was supplied slowly. Reaction was conducted for 4 h, and the reaction liquid was evaporated, concentrated, and recrystallized with precooled hexane. The recrystallization products were washed with hexane and vacuum dried, and then NCA-benzylester was formed.

NCA-benzylester (288.18 mg) and anhydrous dioxane (5.04 mL) were fully mixed in a round bottom flask, sealed, and stirred in 40 °C water bath under nitrogen condition. Dioxane solution with 5 μL sodium methoxide and 16.9 μL methanol was added after the mixture solution was clarified. A clear, colorless, and viscous solution was obtained after stirring for 72 h at 40 °C. Finally, after ethanol was recrystallized, PBLG (PG-ester) was obtained by vacuum drying.

PBLG (100 mg) was dissolved in 4 mL dichloroacetate solution (40 mL/g PBLG) and stirred overnight at 30 °C. Then, 350 μL of acetic acid solution containing 33% HBr was added under stirring. After 1, 3, 5, or 7 h, white precipitates were produced by slowly dropping into precooled hexane. They were placed for 30 min, recrystallized again with acetone, washed three times, and dried at room temperature. The obtained solid was added to 1 N (1.0 mol/L) $NaHCO_3$ solution (pH 7.0–8.0), stirred overnight, and purified by dialyzing (1 kDa). After freeze drying was conducted, white transparent crystal (PGA) was obtained.

PGA (40 mg) was added to DMF and stirred for 0.5 h. Then, 157 mg H-Glu(OtBu)-OtBu·HCl, 48.6 mg HOBt, and 152 mg EDC were added. After stirring was performed for 36 h, recrystallization and washing with 5 mL distilled water were conducted. The freeze-dried product (PGG-ester, 95 mg) and TFA (0.76 mL) were stirred for 5 h, and then TFA was removed by rotary evaporation at 40 °C. The grey transparent foam was dispersed in 0.38 mL TFA (4 mL/g PGG-ester), stirred overnight, and dried in vacuum. The solid was stirred and dissolved in distilled water, purified by dialyzing, and filtered through a 0.45 μm filter membrane. After freeze drying was conducted, PGG was obtained, and ^{1}H-NMR spectra were recorded.

Synthesis of mPEG-SS-PGG

DMF (30 mL) containing 0.75 mmol $mPEG_{5000}$-SS-NH_2 was dispersed dropwise to DMF containing 1.5 mmol PGG and EDC/NHS (1:1 molar ratio) on ice. Stirring was performed for 24 h at 25 °C and then for another 24 h at 60 °C. After filtration, dialysis, and freeze drying were conducted, mPEG-SS-PGG was acquired, and ^{1}H-NMR spectra were recorded.

Synthesis of mPEG-SS-PGG-SS-IR780

Cystamine dihydrochloride (405 mg, 1.80 mmol) and TEA (1.25 mL) were sufficiently dissolved in DMF. Subsequently, IR780 (300 mg, 0.45 mmol) was added. The solution was stirred for 4 h under nitrogen. It was dialyzed against DI water and then freeze dried to obtain IR780-SS-NH_2.

Amphiphilic mPEG-SS-PGG-SS-IR780 conjugates were acquired by grafting IR780-SS-NH_2 to mPEG-SS-PGG through the amidation reaction. In brief, 8.2 g of mPEG-SS-PGG was dispersed in DMSO: H_2O (1: 1, v/v). Following this step, 23 mg of NHS and 31 mg of EDC were mixed and reacted for 2 h. Then, 117.5 mg IR780-SS-NH_2 was added slowly using a stirrer for 24 h under N_2. After reaction, mPEG-SS-PGG-SS-IR780 was dialyzed with methanol for 1 day (MWCO = 3000 Da) and deionized water for an additional 1 day and lyophilized. ^{1}H-NMR spectra were recorded.

The content of conjugated IR780 was determined by fluorescence spectrophotometry with the use of free IR780 as the calibration standard. The mPEG-SS-PGG-SS-IR780 conjugates were accurately weighed and dispersed into DMF. The grafting efficiency (GE%) was measured at 780 nm as follows:

$$GE\% = \text{weight of conjugated IR780}/\text{weight of polymer} - \text{IR780 conjugates} \times 100\%$$

Preparation of mPEG-SS-PGG-SS-IR780/PTXL Micelles

The conjugates and PTXL (2: 1, weight ratio) were dispersed in DMF and dropped in DI water with violent stirring. After dialysis was conducted for 10 h and filtration was performed with 0.45 μm filter membrane, micelle solution was obtained.

Characterization of mPEG-SS-PGG-SS-IR780/PTXL Micelles

Micellar Size and Zeta Potential

The micellar size and zeta potential were measured by dynamic light scattering (DLS, Malvern Instruments, Malvern, UK). The measuring temperature was 25 °C.

Micellar Morphology

A 10 μL sample solution was added to the copper net containing carbon film, and excess liquid was removed using a filter paper. Following drying, 1% phosphotungstic acid was dripped and then dried under infrared light. The morphology was recorded by transmission electron microscopy (TEM, JEM-1230; JEOL, Tokyo, Japan).

Critical Micelle Concentration (CMC)

The CMC of polymers was measured by steady-state fluorescence probe. As a hydrophobic fluorescence probe, pyrene was excited at 340 nm. The ratio (I_{373}/I_{384}) of fluorescence intensity at 373 (I_{373}) and 384 nm (I_{384}) reflected the environment of pyrene. Using the characteristic of pyrene, the lowest concentration of conjugates in water for self-assembly into micelles, ie, CMC, could be determined. In brief, pyrene was dispersed into the micelle solution and diluted to 1.0×10^{-4}, 1.0×10^{-3}, 2.0×10^{-3}, 3.0×10^{-3}, 1.0×10^{-2}, 3.0×10^{-2}, 5.0×10^{-2}, 7.0×10^{-2}, 9.0×10^{-2}, and 1.0×10^{-1} mg/mL. At the same time, pyrene was kept at 6×10^{-6} mol/L. The solution was placed overnight at room temperature and measured using a fluorescence spectrophotometer (LS-55, PerkinElmer, USA). The fluorescence intensity of the solution was measured at 373 and 384 nm. On the basis of the logarithmic diagram of the concentration (log C, mg/mL) as the horizontal coordinate and time as the ordinate, the concentration corresponding to the sharp change of I_{373}/I_{384} was the CMC value.

Drug Loading (DL) and Encapsulation Efficiency (EE)

The DL and EE of PTXL were measured via ultra-centrifugation method.

$$\text{EE } (\%) = \text{actual PTXL loading}/\text{theoretical PTXL loading} \times 100\%$$

$$\text{DL } (\%) = \text{actual PTXL loading}/\text{total weight of nanoparticles} \times 100\%$$

Stability Experiment

The prepared micelles were dispersed into different solutions and vibrated in a 37 °C shaking bed to investigate the stability of mPEG-SS-PGG-SS-IR780/PTXL micelles. Before and after 1 day, the size and PDI were obtained by DLS.

Ultraviolet Visible (UV-Vis) Spectroscopy

IR780, PTXL, and mPEG-SS-PGG-SS-IR780/PTXL MC solutions were separately prepared with methanol. The absorption spectra were measured via UV-vis spectroscopy to determine the optimal detection wavelength.

In-vitro Release Profiles

In-vitro dual stimuli-responsive release of PTXL was performed by membrane dialysis.[42] Five different conditions were designed for the release experiment: (a) 10 mM PBS with 20 μM GSH (pH 7.4), (b) 10 mM PBS with 20 mM GSH (pH 7.4), (c) 10 mM PBS with 20 μM GSH (pH 5.0), (d) 10 mM PBS with 20 mM GSH (pH 5.0), and (e) PTXL in 10 mM PBS with 20 mM GSH (pH 5.0). In general, 1 mg/mL of mPEG-SS-PGG-SS-IR780/PTXL micelle solution was dialyzed (MWCO = 10,000 Da) and then incubated in 30 mL release medium of different conditions in the shaking bed at 37 °C. At the specific time point, 4 mL medium was broken out and 4 mL fresh release solution was added. High-performance

liquid chromatography (C18 column, 4.6×250 mm internal diameter, 5 μm) was used to determine the cumulative release of PTXL at 227 nm. Each experiment was paralleled three times.

Furthermore, the cumulative release of mPEG-SS-PGG-SS-IR780/PTXL MCs in 10 mM PBS (20 mM GSH, pH 5.0) with/without laser irradiation (660 nm, 1 W/cm^2, 60s) was detected using the same methodology.

PDT and PTT Effects of mPEG-SS-PGG-SS-IR780/PTXL MCs

The UV-vis spectra of free IR780 and mPEG-SS-PGG-SS-IR780/PTXL MCs under dark and light were collected to evaluate the photostability. The PTT effect was estimated by irradiating free IR780 and mPEG-SS-PGG-SS-IR780/PTXL MCs while measuring temperature varieties and thermal images. The PDT effect was evaluated by a ROS detection probe (1,3-diphenylisobenzofuran, DPBF).

$$\text{DPBF remaining } (\%) = \text{absorbance post} - \text{irradiation}/\text{absorbance before irradiation} \times 100\%$$

Hemolysis Experiment

Fresh rabbit blood was washed by multiple centrifugations to precipitate the erythrocytes. Red blood cells (RBCs) were diluted into 2% (v/v) suspension with 0.9% saline solution. Then, 500 μL mPEG-SS-PGG-SS-IR780/PTXL MCs or PTXL solution at different concentrations was mixed with 500 μL RBC suspension. All the samples were incubated and centrifuged. The absorbance was recorded at 540 nm. The positive control (deionized water) caused 100% hemolysis, and the negative control (saline) caused 0% hemolysis.

$$\text{Hemolysis rate } (100\%) = (OD_{sample} - OD_{NC})/(OD_{PC} - OD_{NC}) \times 100\%$$

Cell Culture

Human non-small-cell lung cancer cell lines A549 and NCL-H1975, and murine Lewis lung carcinoma (LLC) cells were purchased from Procell Life Science&Technology Co., Ltd. (Wuhan, China). All cells were cultured in RPMI-1640 and incubated in a humidified incubator at 37 °C with 5% CO_2 atmosphere.

In-vitro Cellular Uptake

The internalization of mPEG-SS-PGG-SS-IR780/PTXL MCs, mPEG-PGG-IR780/PTXL MCs + L, and mPEG-SS-PGG-SS-IR780/PTXL MCs + L into A549 and NCL-H1975 cell lines was analyzed by CLSM. In brief, cells were inoculated with 1×10^5 cells per pore on a six-well plate containing circular cover glass and cultured overnight. The cells were cultured with three micelle formulations separately. After they were incubated for 2 h, they were irradiated with an NIR laser and incubated further for 2 h. The cells were washed and fixed at room temperature for 0.5 h with 1 mL of 4% paraformaldehyde solution per pore. After washing with PBS buffer again, the cells were washed with 200 μL Hoechst 33,342 (10 mg/mL) and dyed for 10 min. Finally, the circular cover glass was observed under CLSM.

The uptake was quantified by FCM. Similarly, cells were inoculated on a six-well plate with 1×10^5 cells per well, each containing 2 mL culture medium, and cultured overnight. The cells were cultured with three micelle formulations separately. Two h later, they were irradiated with an NIR laser and then incubated further for 2 h. Then, the cells were digested and washed. Finally, the fluorescence intensity of the suspension cells in 0.5 mL PBS was detected by FCM.

In-vitro Cytotoxicity and Apoptosis Assay

The in-vitro cytotoxicity and apoptosis of free PTXL, mPEG-SS-PGG-SS-IR780/PTXL MCs, mPEG-SS-PGG-SS-IR780 MCs + L, mPEG-PGG-IR780/PTXL MCs + L, and mPEG-SS-PGG-SS-IR780/PTXL MCs + L solutions were evaluated by MTT method and Annexin V-FITC/PI-staining kit, respectively. Cells were seeded into 96-well plates with the density of 5×10^4 cells per well, and the culture medium was 200 μL per well. After incubation was performed, different concentrations of free PTXL and micelle solution were added. After the cells were incubated for 4 h, they were irradiated with an NIR laser and then incubated further for 48 h. Cytotoxicity and apoptosis assays were performed separately.

A fresh medium containing 20 μL MTT was replaced and incubated for 4 h. Then, the blue crystal was dissolved in 150 μL DMSO, and the OD value at 490 nm was measured by a fluorescence microplate reader (Infinite M200 PRO, Tecan, Austria). The cell survival rate was calculated by the following method:

$$\text{Cell viability } (\%) = \text{OD}_{\text{treated}}/\text{OD}_{\text{control}} \times 100\%$$

where $\text{OD}_{\text{treated}}$ and $\text{OD}_{\text{control}}$ represent the absorbance of the sample and the control, respectively.

For apoptosis assay, cells were digested, washed, and stained with Annexin V-FITC/PI. The apoptosis was analyzed by FCM.

Mitochondria-Targeting Ability and Dysfunction Tests

A549 cells were treated with mPEG-SS-PGG-SS-IR780/PTXL MCs and mPEG-PGG-IR780/PTXL MCs with or without NIR. After 4 h, the cells were collected to evaluate the mitochondrial localization, mitochondrial membrane potential (MMP), ROS, and ATP contents by using a Mito-tracker green kit (Biyuntian, Hangzhou, China), an MMP assay kit with JC-1 (Elabscience, Wuhan, China), an ROS assay kit (Biyuntian, Hangzhou, China), and an ATP assay kit (Solaibao, Beijing, China), respectively.

In-vitro Inducing ICD

Free PTXL, mPEG-SS-PGG-SS-IR780/PTXL MCs, mPEG-SS-PGG-SS-IR780 MCs, and mPEG-PGG-IR780/PTXL MCs with or without NIR were co-incubated with A549 cells for 4 h. The cells were incubated with CRT and HMGB-1 antibody (Biyuntian, Hangzhou, China) separately and then examined via FCM. Meanwhile, the extracellular release of ATP was investigated using an ATP assay kit. The CFDA-SE probe (Biyuntian, Hangzhou, China) was used to determine the T cell proliferation.

Animal Experiments

Male Balb/c mice were obtained from Beijing Vital River Laboratory Animal Technology Co., ltd. (Beijing, China). Animal experiments were performed following the National Institute of Health Guide for the Care and Use of Laboratory Animals in China and were approved by the Experimental Animals Administrative Committee of Binzhou Medical University.

In-vivo Fluorescence and PTT Imaging

Tumor-bearing mice were injected with free IR780 and mPEG-SS-PGG-SS-IR780/PTXL MCs by tail vein injection. At predetermined time points, fluorescence and PTT imaging were recorded by a small animal PET imager system (IVIS spectrum, PE, USA) and a thermal infrared camera (FLIR E8, USA), respectively.

In-vivo Pharmacodynamic and Biosafety Experiments

Five groups of LLC tumor-bearing mice were set (n = 5) and injected via tail vein with saline, free PTXL, mPEG-SS-PGG-SS-IR780/PTXL MCs, mPEG-PGG-IR780/PTXL MCs + L, and mPEG-SS-PGG-SS-IR780/PTXL MCs + L. In accordance with the fluorescence imaging results, 12 h after dosing, tumor tissues were treated with laser for 5 min. Treatments were carried out every 4 days. Body weight and tumor volume were recorded every second day. After treatment for 21 days, blood routine tests (WBC, RBC, PLT, and HGB), blood biochemistry tests (AST, ALT, Cr, and BUN), and ELISA serum (TNF-α, IFN-γ, and IL-6) assays from various groups were conducted. The major organs and tumors were removed for further H&E staining and effector T cell detection.

Statistical Analysis

SPSS 22.0 software (IBM Corp., Armonk, NY, USA) was used for all statistical analyses. Normally distributed data were presented as mean ± SD and obtained from at least three independent experiments. Averages and multiple groups were analyzed by Student's *t* test and ANOVA. The statistical significance of comparative data was established at P-value < 0.05.

Results and Discussion

Synthesis and Characterization of mPEG-SS-PGG-SS-IR780

The synthesis of dual stimuli-responsive polymer mPEG-SS-PGG-SS-IR780 via a series of several steps was successful (Figure 1), and ^{1}H-NMR was further used to verify the successful synthesis. According to Figure 2A, the strong peak at 3.54 and 2.88 ppm could be assigned to the proton peaks of methylene and methoxy on mPEG, respectively. The peaks in the range of 2.97–3.08 and 1.72 ppm represent the presence of cystamine hydrogen proton, thereby confirming the synthesis of mPEG-SS-NH_2. The proton peaks at 4.28, 4.16, 2.43, 2.13, and 1.93 ppm demonstrated the synthesis of PGG. The integral values of proton on tertiary carbon (b, 43.2) and secondary carbon (c, 171.7) indicated that 8–9 mPEG chains were grafted with each PGG (Figure 2B). The peaks at 7.3–8.12 ppm could be attributed to the aromatic protons

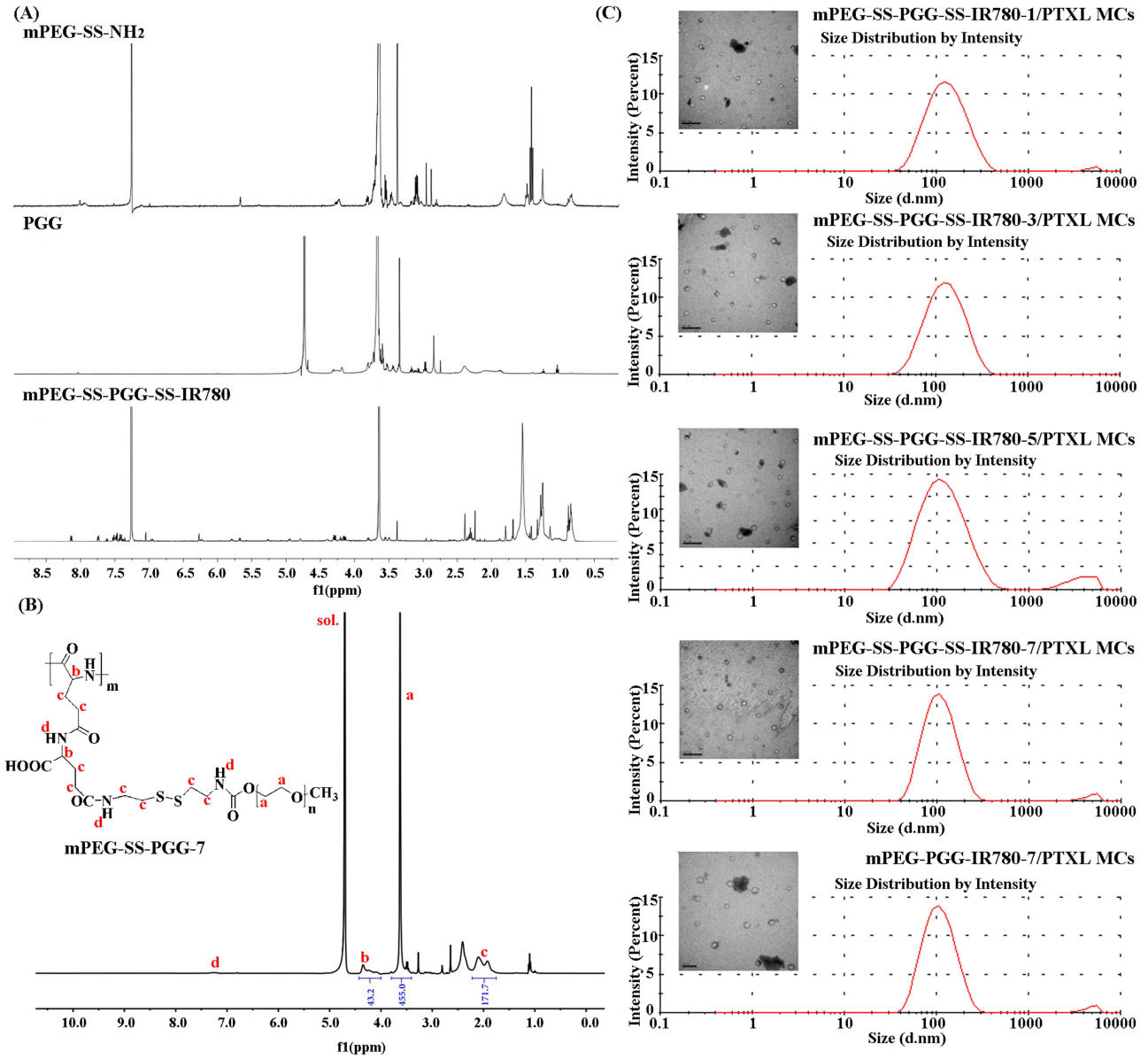

Figure 2 (**A**) ^{1}H-NMR spectra of mPEG-SS-NH_2 in $CDCl_3$, PGG in D_2O, and mPEG-SS-PGG-SS-IR780 in $CDCl_3$. (**B**) ^{1}H-NMR spectra of mPEG-SS-PGG-7 in D_2O (hydrolysis for 7 h). (The red text represented the characteristic hydrogen atoms of mPEG-SS-PGG-7 as well as their chemical shifts.) (**C**) Diameter and size distribution of mPEG-SS-PGG-SS-IR780-1/PTXL MCs (hydrolysis for 1 h), mPEG-SS-PGG-SS-IR780-3/PTXL MCs (hydrolysis for 3 h), mPEG-SS-PGG-SS-IR780-5/PTXL MCs (hydrolysis for 5 h), mPEG-SS-PGG-SS-IR780-7/PTXL MCs (hydrolysis for 7 h), and mPEG-PGG-IR780-7/PTXL MCs (hydrolysis for 7 h) by DLS and TEM. Scale bar: 0.5 μm.

Abbreviations: ^{1}H-NMR, ^{1}H-nuclear magnetic resonance; $CDCl_3$, deuterium chloroform; PGG, poly(L-γ-glutamylglutamine); D_2O, deuteroxide; PTXL, paclitaxel; DLS, dynamic light scattering; TEM, transmission electron microscopy.

of IR780 (Figure 2A). The results proved that IR780 was grafted to polymer and mPEG-SS-PGG-SS-IR780 was synthesized. The GE% of IR780 was confirmed by fluorescence spectrophotometry as 5.43%.

Characterization of mPEG-SS-PGG-SS-IR780/PTXL Micelles

As an amphiphilic polymer, the synthesized mPEG-SS-PGG-SS-IR780/PTXL conjugate could self-assemble into micelles. The size distribution and morphology were measured by DLS and TEM (Figure 2C and Table 1). mPEG-SS-PGG-SS-IR780-1, mPEG-SS-PGG-SS-IR780-3, mPEG-SS-PGG-SS-IR780-5, mPEG-SS-PGG-SS-IR780-7, and mPEG-PGG-IR780-7 were prepared by hydrolysis of polymers containing disulfide bonds and those without disulfide bonds for 1, 3, 5, or 7 h, respectively. The results indicated that all the micelles were spherical with narrow particle size distribution. The physicochemical properties were summarized in Table 1. As the hydrolysis time extended, the size distribution became narrower and the average size became smaller. The CMC decreased with decreasing molecular weight, indicating that micelles tended to be more stable with smaller molecular weight (Table 1 and Figure 3A). mPEG-SS-PGG-SS-IR780-7/PTXL MCs showed the highest DL% and EE% of 5.62 ± 0.15% and 88.63 ± 1.58%, respectively. Thus, 7 h was regarded as the optimal hydrolysis time.

Furthermore, for mPEG-SS-PGG-SS-IR780/PTXL MCs, no significant difference in particle size and PDI was observed before and after storage (Table 2), demonstrating the colloidal stability serum stability of this nano-micelle. This finding may be related to the core–shell structure and the strong hydrophobic interaction forming a tight core, which was not susceptible to be influenced by enzymes or water, to avoid the destruction of micelle structures and the leakage of drugs in the blood circulation.

The UV-vis spectra showed sharp absorption peaks of IR780 at 785 nm, while PTXL had maximum absorption at 227 nm (Figure 3B). The mPEG-SS-PGG-SS-IR780/PTXL MCs revealed two absorption bands at 227 and 647 nm, representing the absorption peak of PTXL and a blue-shift absorption peak of IR780, respectively, which further confirmed the successful synthesis of mPEG-SS-PGG-SS-IR780 polymer. Considering the absorption maximum wavelengths, 808 nm laser was used for IR780, and 660 nm laser was used for mPEG-SS-PGG-SS-IR780/PTXL MCs.

In-vitro Release Profiles

Much literature has been devoted to designing drug carriers that could control release and effective release at the indicated site to improve the therapeutic utility.[43,44] In the present study, dialysis method was used to simulate intracellular environment, and the release behavior was studied under the synergistic action of the two stimuli. As shown in Figure 3C, the release profiles presented controlled release kinetics without burst drug release. The release rate and accumulative release (%) of PTXL increased significantly under the release condition containing 10 mM GSH, indicating that the reductive sensitive release behavior of the micelles could appear rapidly under the special high reduction potential energy in the intracellular environment. Meanwhile, the release of PTXL obviously increased under low pH, indicating that the micelles had acid sensitivity. Under low pH or high GSH environment, redox-sensitive disulfide bond and pH-sensitive amide bond could be broken and caused mPEG-SS-PGG-SS-IR780/PTXL MCs disintegration. PTXL was released from the hydrophobic core of the micelles, which achieved the dual stimuli-responsive release behavior.

Table 1 Characterization of Micelles (Mean ± SD, n = 3)

Sample	Size (nm)	PDI	Zeta Potential (mV)	CMC (mg/mL)	DL (%)	EE (%)
mPEG-SS-PGG-SS-IR780-1/PTXL MCs	115.4±1.43	0.220±0.36	−21.8±0.50	0.015	3.63±0.17	81.91±2.1
mPEG-SS-PGG-SS-IR780-3/PTXL MCs	112.2±0.92	0.203±0.24	−14.8±0.23	0.011	4.91±0.11	84.19±1.41
mPEG-SS-PGG-SS-IR780-5/PTXL MCs	98.7±0.96	0.195±0.19	−18.4±0.34	0.0098	5.17±0.02	85.13±0.32
mPEG-SS-PGG-SS-IR780-7/PTXL MCs	92.8±1.21	0.178±0.23	−16.3±0.78	0.0084	5.62±0.15	88.63±1.58
mPEG-PGG-IR780-7/PTXL MCs	93.5±1.33	0.189±0.16	−17.6±0.43	0.0089	5.77±0.21	89.04±2.34

Abbreviations: SD, standard deviation; PDI, polydispersity index; CMC, critical micelle concentration; DL, drug loading; EE, encapsulation efficiency; PTXL, paclitaxel.

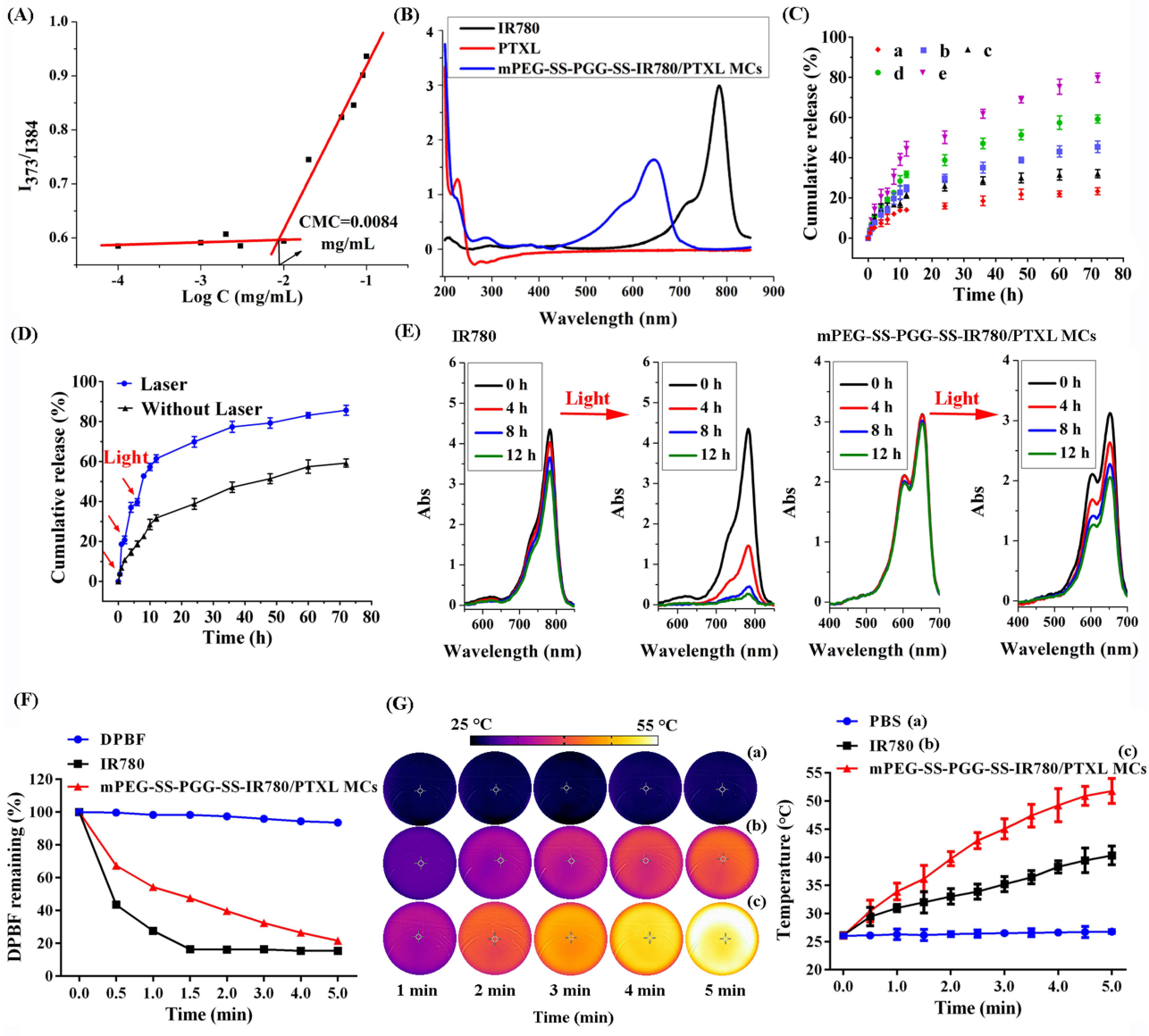

Figure 3 (**A**) CMC of mPEG-SS-PGG-SS-IR780/PTXL MCs. (**B**) UV-vis spectra of IR780 iodide, PTXL, and mPEG-SS-PGG-SS-IR780/PTXL MC solutions. (**C**) Controlled release profiles of mPEG-SS-PGG-SS-IR780/PTXL MCs with or without laser irradiation (red arrows indicated laser irradiation). Data were means ± SD (n = 3). (**D**) In-vitro PTXL release profiles from the mPEG-SS-PGG-SS-IR780/PTXL MCs at (a) 10 mM PBS with 20 μM GSH (pH 7.4), (b) 10 mM PBS with 20 mM GSH (pH 7.4), (c) 10 mM PBS with 20 μM GSH (pH 5.0), (d) 10 mM PBS with 20 mM GSH (pH 5.0), and (e) PTXL in 10 mM PBS with 20 mM GSH (pH 5.0). Data were means ± SD (n = 3). (**E**) UV-vis spectra of free IR780 and mPEG-SS-PGG-SS-IR780/PTXL MCs in the dark or exposed to light at 0, 4, 8, and 12 h. (**F**) Singlet oxygen generation abilities of IR780 and mPEG-SS-PGG-SS-IR780/PTXL MCs under NIR laser irradiation (1 W/cm^2) for different period times. (**G**) Thermal images and temperature elevation profiles of PBS (a), IR780 (b) and mPEG-SS-PGG-SS-IR780/PTXL MCs (c) under NIR laser irradiation (1 W/cm^2, 5 min). Data were means ± SD (n = 3).

Abbreviations: CMC, critical micelle concentration; UV-vis, ultraviolet-visible spectroscopy; SD, standard deviation; PBS, phosphate buffered saline; GSH, glutathione; NIR, near-infrared.

Furthermore, mPEG-SS-PGG-SS-IR780/PTXL MCs were incubated in 10 mM PBS (20 mM GSH, pH 5.0) with or without laser (660 nm, 1 W/cm^2, 60s), to investigate the controlled release property with laser. Following 60s of light irradiation, a significantly accelerated PTXL release rate was observed (Figure 3D). Ultimately, over 80% PTXL was released from the mPEG-SS-PGG-SS-IR780/PTXL MCs at 72 h after three cycles of irradiation. The results showed that NIR laser irradiation successfully triggered fast drug release.

Table 2 Size and Distributions of mPEG-SS-PGG-SS-IR780/PTXL MCs Incubated at Different Conditions

Conditions	Before Storage		After Storage	
	Size (nm)	PDI	Size (nm)	PDI
Saline	94.6 ± 1.04	0.166 ± 0.26	97.4 ± 2.45	0.192 ± 0.21
50% FBS	111.29 ± 2.18	0.205 ± 0.17	123.19 ± 2.98	0.265 ± 0.25

Abbreviation: PDI, polydispersity index.

PDT and PTT Effects of mPEG-SS-PGG-SS-IR780/PTXL MCs

The photostability of mPEG-SS-PGG-SS-IR780/PTXL MCs was investigated to obtain excellent phototherapeutic and fluorescence imaging effect. For the UV-vis spectra of IR780, the absorption tended to decrease after 12 h in darkness (Figure 3E). When exposed to light, the photodegradation was more obvious. Surprisingly, the photostability of mPEG-SS-PGG-SS-IR780/PTXL MCs markedly increased either in the dark or in the light, thus further supporting the subsequent treatment study.

Subsequently, the PTT and PDT effects of mPEG-SS-PGG-SS-IR780/PTXL MCs were evaluated. The generation of $^1O_2$ was confirmed using DPBF as probe. DPBF remaining was inversely related to the ability of photosensitizers to produce $^1O_2$. The variation of DPBF remaining between mPEG-SS-PGG-SS-IR780/PTXL MCs and IR780 was less than 10%, indicating that the mPEG-SS-PGG-SS-IR780/PTXL MCs produced large amounts of $^1O2$ as efficiently as IR780 (Figure 3F). Photothermal properties were also evaluated by examining the temperature rise. As shown in Figure 3G, under NIR laser irradiation, the temperature of free IR780 only increased at about 10 °C within 5 min, whereas the mPEG-SS-PGG-SS-IR780 /PTXL MCs showed distinct increases (near 25 °C). The thermal images were observed (Figure 3G), which was in accordance with the above mentioned results. A notable detail that the excellent PDT and PTT properties benefited from the improved photostability, indicating that mPEG-SS-PGG-SS-IR780/PTXL MCs have great potential as phototherapy agents.

Hemolysis Experiment

Hemolysis is commonly used for intravenous safety evaluation to nanoparticles. No hemolysis was detected, and the hemolysis rate was below 5% in the investigated concentration range (50–800 μg/mL), indicating that mPEG-SS-PGG-SS-IR780/PTXL MCs were relatively safe for intravenous injection (Figures 4A and B).

In-vitro Cellular Uptake

Efficient cellular uptake is the foundation to execute antitumor response. The cellular uptake of IR780-micelles could be observed by CLSM. In A549 and NCL-H1975 cells, the mPEG-SS-PGG-SS-IR780/PTXL MCs + L group showed the strongest red fluorescent signals (Figure 4C), suggesting that local heat treatment could be generated by IR780 after NIR irradiation, thus increasing cell membrane permeability towards micelles and enhancing cellular uptake effectively. Compared with the mPEG-PGG-IR780/PTXL MCs + L group (without disulfide bonds), the mPEG cleavage in response to oxidation-reduction responsiveness facilitated tumor cell endocytosis to mPEG-SS-PGG-SS-IR780/PTXL MCs + L. Quantitative analysis of cellular uptake was performed by FCM. These results of FCM were consistent with those of CLSM (Figure 4D).

In-vitro Cytotoxicity and Apoptosis Assay

MTT assay was used to assess the treatment effect on A549 and NCL-H1975 cell lines to investigate the PTT/PDT/CT combination therapy of mPEG-SS-PGG-SS-IR780/PTXL MCs. The biocompatibility of mPEG-SS-PGG-SS-IR780 MCs was proven in a biocompatibility experiment (Figure 5A). The A549 and NCL-H1975 cells treated with all formulations showed concentration- and dose-dependent cytotoxicity effects (Figures 5B and C). The micelle groups (except mPEG-SS-PGG-SS-IR780/PTXL MCs + L group) demonstrated a relatively weaker cytotoxicity than the free PTXL group, probably due to the passive-diffusion mechanism of free PTXL, however, endocytosis mechanism of micelles. After treatment by mPEG-SS-PGG-

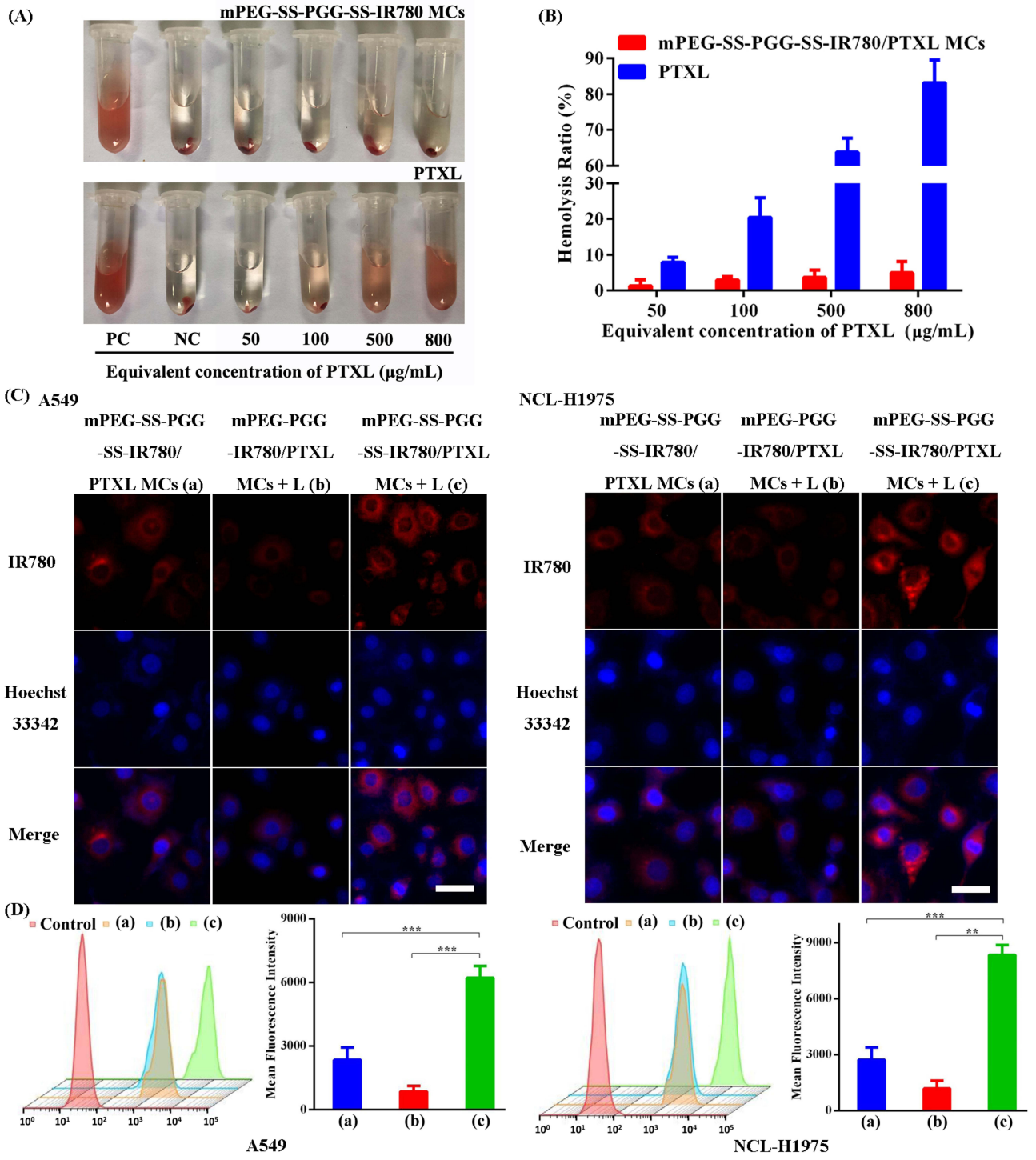

Figure 4 Hemolysis ratio (**A**) and photos (**B**) of red blood cells after being cultured with PTXL and mPEG-SS-PGG-SS-IR780/PTXL MCs at various concentrations (n = 5). (**C**) CLSM images of A549 and NCL-H1975 cells incubated with different formulations. Scale bar: 20 μm. (**D**) Cell uptake of control, mPEG-SS-PGG-SS-IR780/PTXL MCs (a), mPEG-PGG-IR780/PTXL MCs + L (b), and mPEG-SS-PGG-SS-IR780/PTXL MCs + L (c) analyzed by FCM. Mean fluorescence intensities showing the IR780 intensity inside A549 cells incubated with mPEG-SS-PGG-SS-IR780/PTXL MCs (a), mPEG-PGG-IR780/PTXL MCs + L (b), and mPEG-SS-PGG-SS-IR780/PTXL MCs + L (c). Data were means ± SD (n = 3, $^{**}P < 0.01$, $^{***}P < 0.001$).

Abbreviations: PTXL, paclitaxel; CLSM, confocal laser scanning microscope; FCM, flow cytometry.

SS-IR780/PTXL MCs + L, the cell viability was only 28%, which was evidently less than that (67%) without disulfide bonds (mPEG-PGG-IR780/PTXL MCs + L group). The strong cytotoxic activity could be likely associated with mPEG cleavage causing effective cellular uptake of mPEG-SS-PGG-SS-IR780/PTXL MCs under NIR laser irradiation. Micelle disintegration

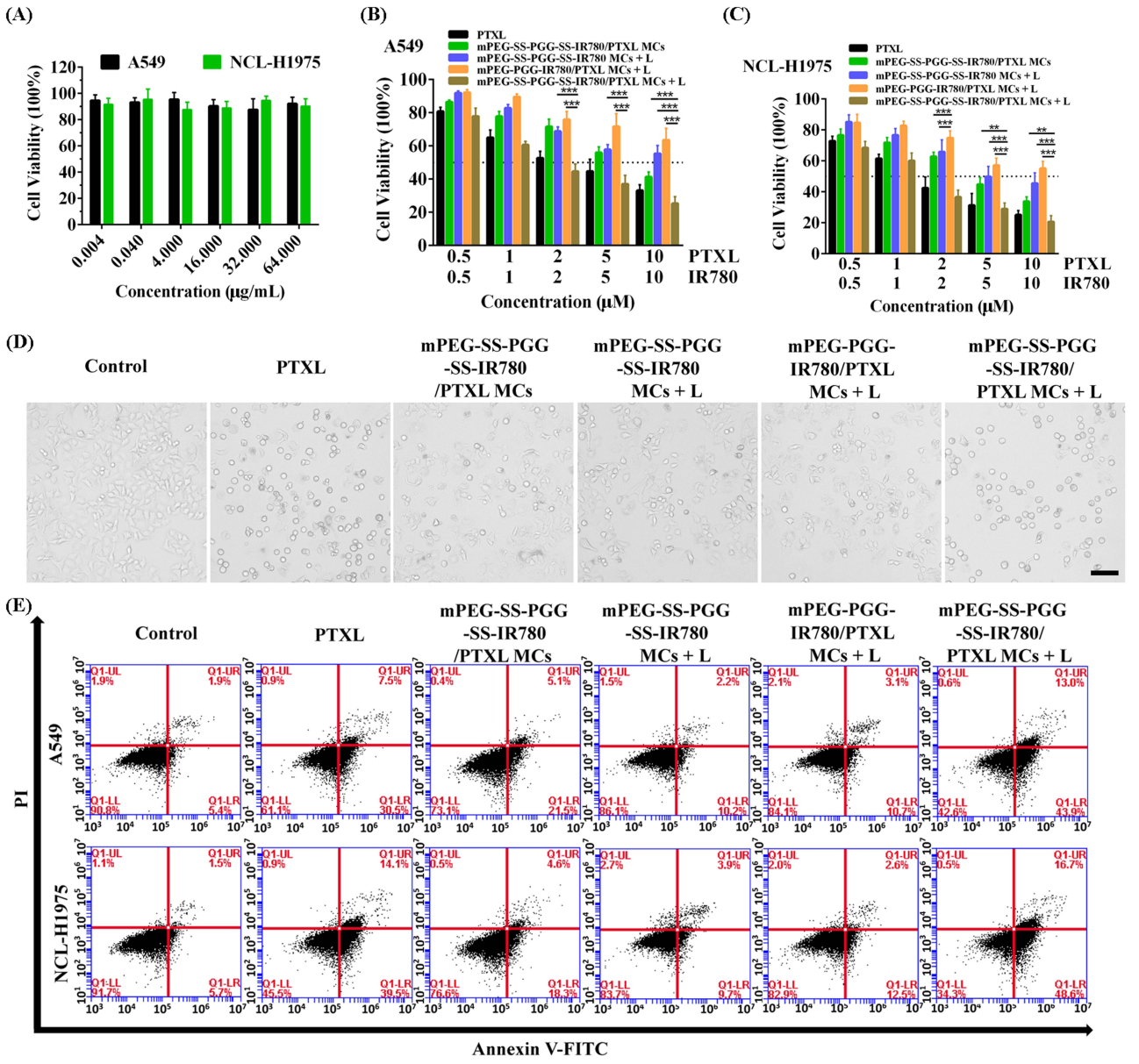

Figure 5 (**A**) Biocompatibility study of mPEG-SS-PGG-SS-IR780 MCs against A549 and NCL-H1975 cells for 72 h (equivalent to the equivalent concentration of PTXL, n = 6). Cytotoxicity analysis of different formulations on A549 (**B**) and NCL-H1975 cells (**C**) for 48 h through MTT assay (n = 6, $^{**}P < 0.01$, $^{***}P < 0.001$). (**D**) Changes in A549 cell viability and morphology, as observed with an inverted microscope. Scale bar: 50 μm. (**E**) Flow cytometric cell apoptosis assay of Annexin V-FITC and PI double-stained A549 cells after different treatments.

Abbreviations: FITC, fluorescein isothiocyanate; PI, propidium iodide.

resulting from dual stimuli-responsive bonds breaking may also be one of the reasons. Under laser irradiation, the mPEG-PGG-IR780/PTXL MC group (mPEG-PGG-IR780/PTXL MCs + L) exhibited better cytotoxicity than the unilluminated group (mPEG-PGG-IR780/PTXL MCs). This confirms that PTT/PDT/CT combination played an adequate therapeutic role. And the heat-induced destruction of micelles facilitating release of the drug and heat-induced cell membrane permeability enhanced the cellular uptake, both enhancing the treatment effect. The morphology of A549 cells in the mPEG-PGG-IR780/PTXL MCs + L group had obvious cell shrinkage, cytomorphosis, and cytoplasm area decrease (Figure 5D).

The cytotoxicity research was further verified by Annexin V-FITC/PI double staining to investigate cell apoptosis (Figure 5E). The cell apoptosis rate caused by mPEG-SS-PGG-SS-IR780/PTXL MCs + L group was up to 65.3%, which was significantly higher than that of other groups. Therefore, mitochondrion-targeted PTT/PDT/CT combination micelles were able to promote apoptosis.

Mitochondria-Targeting Ability and Dysfunction Tests

The subcellular localization of photosensitizers is especially important on the effectiveness of phototherapy. The mitochondria are considered as one of the most sensitive targets for PTT and PDT damage.[45,46] Thus, increasing the concentration of photosensitizers in the mitochondria could induce more efficient apoptosis, improve phototherapy effect, and boost the antitumor immune response. The red fluorescence of the mPEG-SS-PGG-SS-IR780/PTXL MCs + L group coincided well with the green fluorescence, confirming the efficient capability of mitochondrial targeting, which was closely related to the efficient cellular uptake (Figure 6A).

This mitochondrial targeting ability was beneficial to improve the photo-induced cytotoxicity because the mitochondria are the principal site of ROS generation and they are vulnerable to ROS and hyperthermia attack. NIR laser-activated

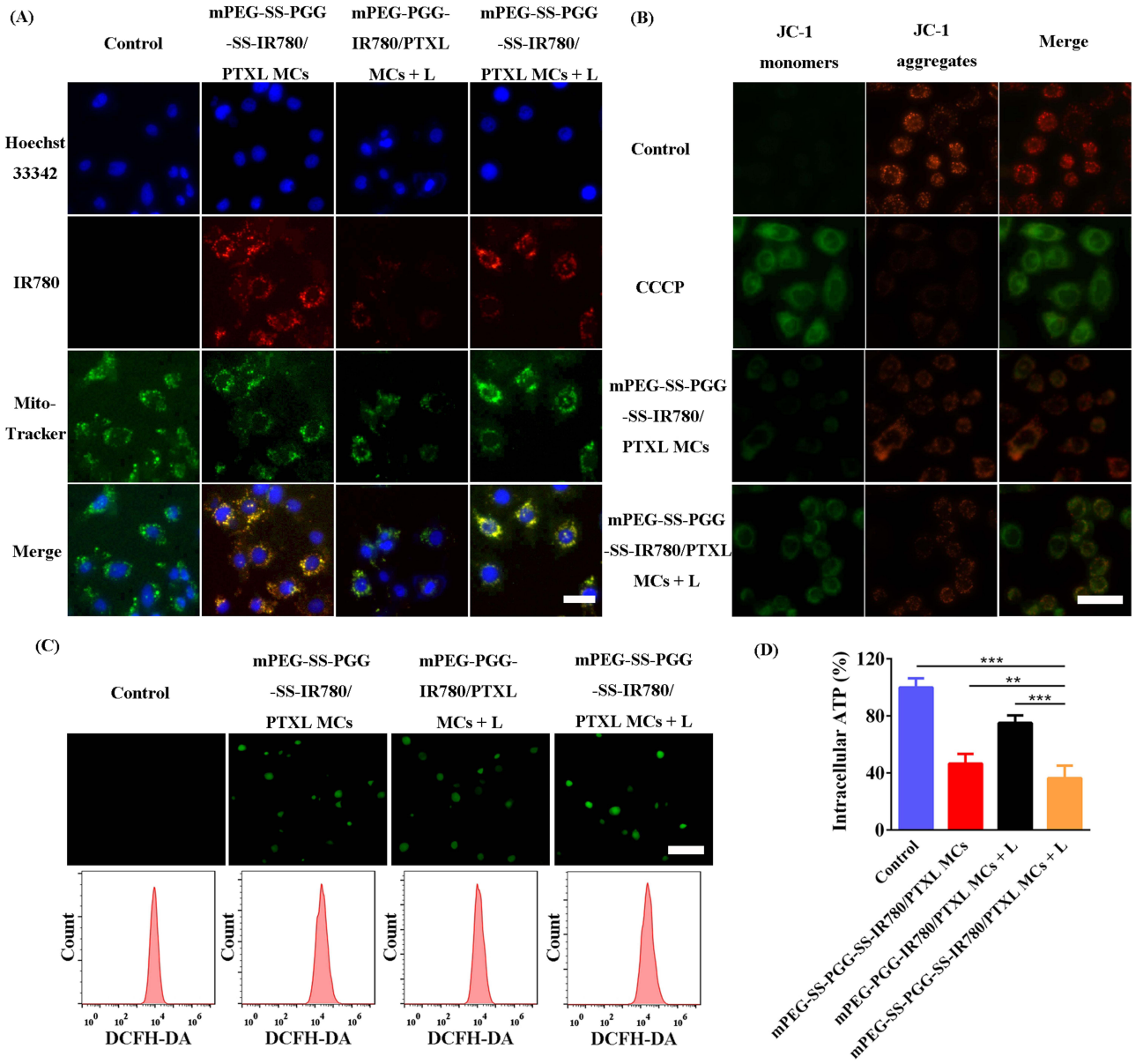

Figure 6 (**A**) Mitochondrial targeting ability detection. Scale bar = 20 μm. Red fluorescence represented photosensitizer, green fluorescence represented the mitochondria, and blue fluorescence represented the nucleus. The yellow channel represented colocalization of red fluorescence of the photosensitizer and green fluorescence of the mitochondria. (**B**) Fluorescence images of A549 cells stained with MMP probe JC-1 after various treatments. Scale bar = 50 μm. (**C**) Fluorescence images of A549 cells stained with ROS probe DCFH-DA after various treatments. Scale bar = 100 μm. Fluorescence intensities of A549 cells stained with ROS probe DCFH-DA measured by FCM. (**D**) Intracellular ATP levels of A549 cells after various treatments (n = 6, $^{**}P < 0.01$, $^{***}P < 0.001$).

Abbreviations: MMP, mitochondrial membrane potential; ROS, reactive oxygen species; DCFH-DA, 2',7'-dichlorodihydrofluorescein diacetate; FCM, flow cytometry; ATP, adenosine triphosphate.

targeted mitochondrial accumulation could provoked mitochondrial dysfunction. From Figure 6B, the control group showed much less green fluorescence than red, indicating normal mitochondrial status. However, in the mPEG-SS-PGG-SS-IR780/PTXL MCs + L group, the green fluorescence increased significantly and the red fluorescence decreased significantly, which confirmed the loss of MMP and the destruction of mitochondrial membrane.

In the presence of ROS, non-fluorescent DCFH-DA reacts and converts to fluorescent 2',7'-dichlorofluorescein (DCF). Therefore, a DCFH-DA fluorescent probe was applied to detect ROS levels. The strongest ROS fluorescence signals indicated that mPEG-SS-PGG-SS-IR780/PTXL MCs could produce substantial ROS to kill tumor cells upon laser irradiation (Figure 6C).

Mitochondrial dysfunction could directly lead to decreased intracellular ATP synthesis. mPEG-SS-PGG-SS-IR780 /PTXL MCs + L group down-regulated intracellular ATP levels by > 60% (Figure 6D). Collectively, these results taken together confirmed the mitochondrion-targeted damage by mPEG-SS-PGG-SS-IR780/PTXL MCs under laser irradiation.

In-vitro Inducing ICD

Encouraged by the comforting mitochondrion-targeting combined therapy effect of PTT, PDT, and CT, this study hypothesized that mPEG-SS-PGG-SS-IR780/PTXL MCs with laser irradiation could trigger potent antitumor immune response via inducing ICD. The induction of ICD is related to the release of DAMPs, such as CRT, HMGB-1, and ATP, which, in turn, stimulates T cell activation, proliferation, and differentiation. As provided in Figures 7A–F, the mPEG-SS

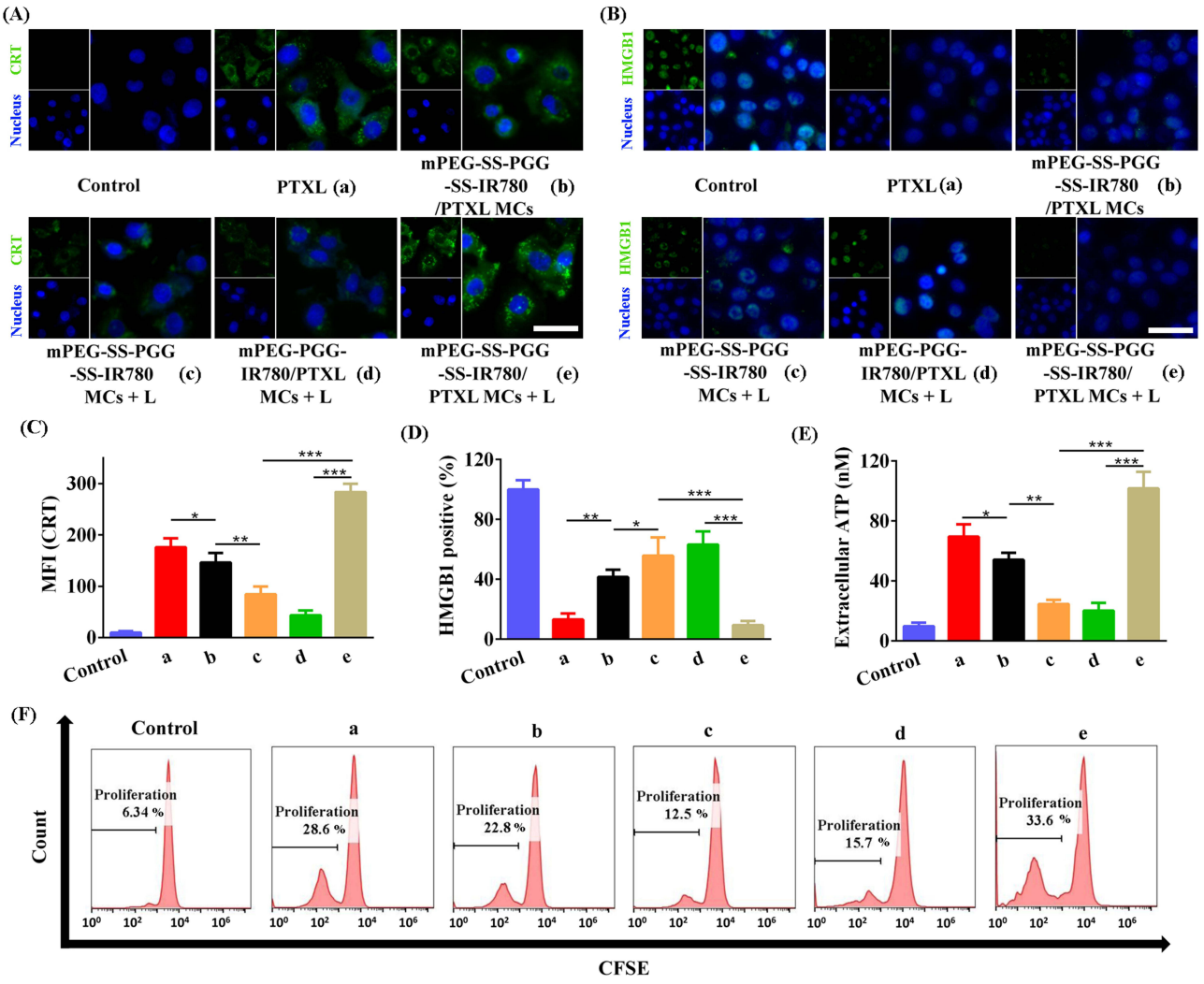

Figure 7 Immunofluorescent staining of (**A**) CRT (green) and (**B**) HMGB-1 (green), both on A549 cells. Scale bar: 20 μm. Quantitative analysis of (**C**) CRT and (**D**) HMGB-1. Data were presented as mean ± SD (n = 3, *$P < 0.05$, **$P < 0.01$, ***$P < 0.001$). (**E**) Extracellular ATP detection of A549 cells. Data were presented as mean ± SD (n = 3, *$P < 0.05$, **$P < 0.01$, ***$P < 0.001$). (**F**) Proliferation of T cells co-incubated with different treated cancer cells.
Abbreviations: CRT, calreticulin; HMGB-1, high mobility group box 1 protein; SD, standard deviation.

-PGG-SS-IR780/PTXL MCs + L group showed significantly increased CRT exposure, reduced HMGB-1 expression, enhanced ATP release and T cell proliferation. The above results supported that mPEG-SS-PGG-SS-IR780/PTXL MCs could result in an efficient ICD after exposure to laser and then augment antitumor immune responses, to further promoted the toxicity and apoptosis.

In-vivo Fluorescence and PTT Imaging

Free IR780 and mPEG-SS-PGG-SS-IR780/PTXL MCs were injected to LLC tumor-bearing mice to evaluate the distribution and tumor accumulation of the nanoparticles in-vivo and confirm the in-vivo imaging capacity. The fluorescence signals were recorded at different time points post-administration by a small animal imaging system. As shown in Figures 8A and S1A, IR780 was accumulated in the tumor from 4 h to 12 h post-injection, but then it disappeared rapidly. For mPEG-SS-PGG-SS-IR780/PTXL MCs, the fluorescence intensity at the tumor enhanced over time and remained until up to 48 h, consistent with

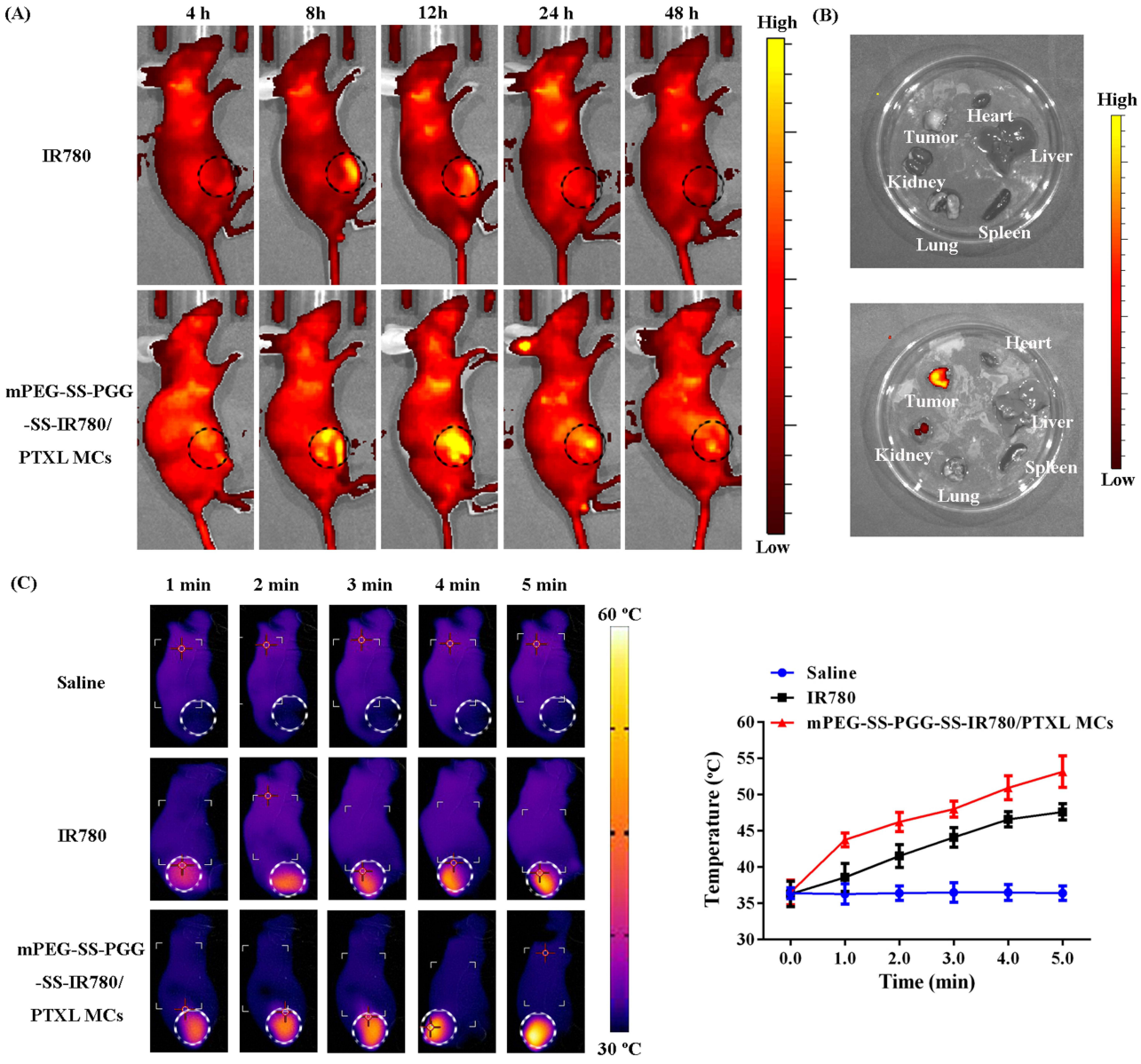

Figure 8 (**A**) In-vivo fluorescence images of LLC tumor-bearing mice after 4, 8, 12, 24, and 48 h of intravenous injection of IR780 and mPEG-SS-PGG-SS-IR780/PTXL MCs. (**B**) Ex-vivo fluorescence images of dissected major organs (heart, liver, spleen, lung, and kidney) and tumor at 48 h. (**C**) Thermal images of LLC tumor-bearing mice receiving intravenous injection of saline, free IR780, or mPEG-SS-PGG-SS-IR780/PTXL MCs upon laser irradiation. And changes in temperature of tumors upon laser irradiation. Data were presented as mean ± SD (n = 3).

the results of the ex-vivo imaging (Figures 8B and S1B). Overall, mPEG-SS-PGG-SS-IR780/PTXL MCs had significantly higher fluorescence signal than IR780 in the tumor site, indicating the strong tumor accumulation ability of mPEG-SS-PGG-SS-IR780/PTXL MCs. This finding could be explained by the EPR effect and dual stimuli-responsive micelles. In addition, the greatest fluorescence signal of mPEG-SS-PGG-SS-IR780/PTXL MCs on the tumor site was obtained at 12 h post-injection. Therefore, 12 h was chosen for laser irradiation after intravenous administration.

Subsequently, the temperature changes in mouse tumors under NIR light irradiation were recorded using a thermal infrared camera, and the temperature rise curve was plotted. As show in Figure 8C, with the extension of irradiation time,

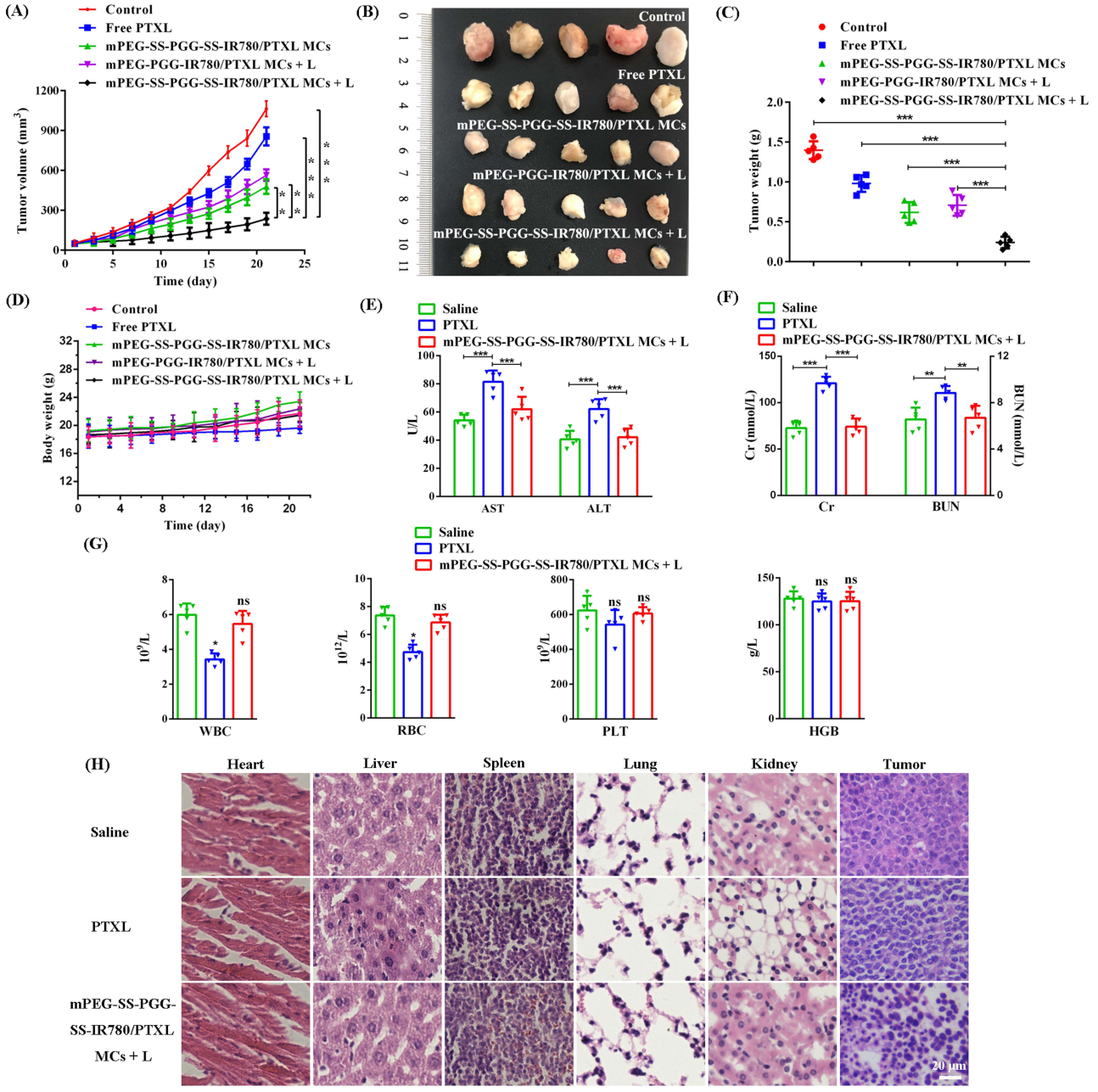

Figure 9 (**A**–**D**) Anti-tumor efficacy in LLC xenograft models: tumor growth, photographs of tumor tissues, tumor weight, and body weight profiles under different treatments. The mice were treated with various formulations by i.v. injection at a dose of 10 mg/kg PTXL (n = 5, $^{**}P < 0.01$, $^{***}P < 0.001$). (**E**–**G**) Evaluation of AST, ALT, Cr, BUN, WBC, RBC, PLT, and HGB levels upon treatment with saline, PTXL, and mPEG-SS-PGG-SS-IR780/PTXL MCs + L (n = 5, $^{*}P < 0.05$, $^{**}P < 0.01$, $^{***}P < 0.001$). (**H**) Image of H&E assays in the heart, liver, spleen, lung, kidney, and tumor after treatment with various formulations over 21 days. Scale bars = 20 μm.

Abbreviations: PTXL, paclitaxel; AST, aspartate aminotransferase; ALT, alanine aminotransferase; Cr, creatinine; BUN, blood urea nitrogen; WBC, white blood cell; RBC, red blood cell; PLT, platelets; HGB, hemoglobin.

negligible tumor temperature changes in the saline group were presented. The in-vivo distribution of IR780 showed a degree of accumulation at the tumor site, and the temperature increased to 11.32 °C at the tumor site. However, due to the efficient tumor accumulation capacity of mPEG-SS-PGG-SS-IR780/PTXL MCs, the increases in tumor temperature were about 10 °C and 20 °C after 2 and 5 min of irradiation, respectively. These results were consistent with those of the in-vitro photothermal conversion experiment and corresponded with those of the in-vivo distribution experiment, indicating the excellent photothermal effect of mPEG-SS-PGG-SS-IR780/PTXL MCs in-vivo.

In-vivo Pharmacodynamic and Biosafety Experiments

The tumor-bearing mice were randomly divided into five groups (n = 5 per group), namely, control group, free PTXL group, mPEG-SS-PGG-SS-IR780/PTXL MC group, mPEG-PGG-IR780/PTXL MCs + L group, and mPEG-SS-PGG-SS-IR780 /PTXL MCs + L group, to investigate the antitumor activities. Figures 9A–C illustrate the tumor volume variation per group, photographs of tumor tissues, and the average tumor weight in each group, respectively. Compared with the control group (no inhibitory effect on tumor growth), the free PTXL group had certain inhibitory effect on tumor growth in mice, reflecting the CT effect of PTXL. Among all the micelle treatment groups, the mPEG-SS-PGG-SS-IR780/PTXL MCs + L group demonstrated the smallest tumor volumes of mice and the best therapeutic effects. The results may be attributed to

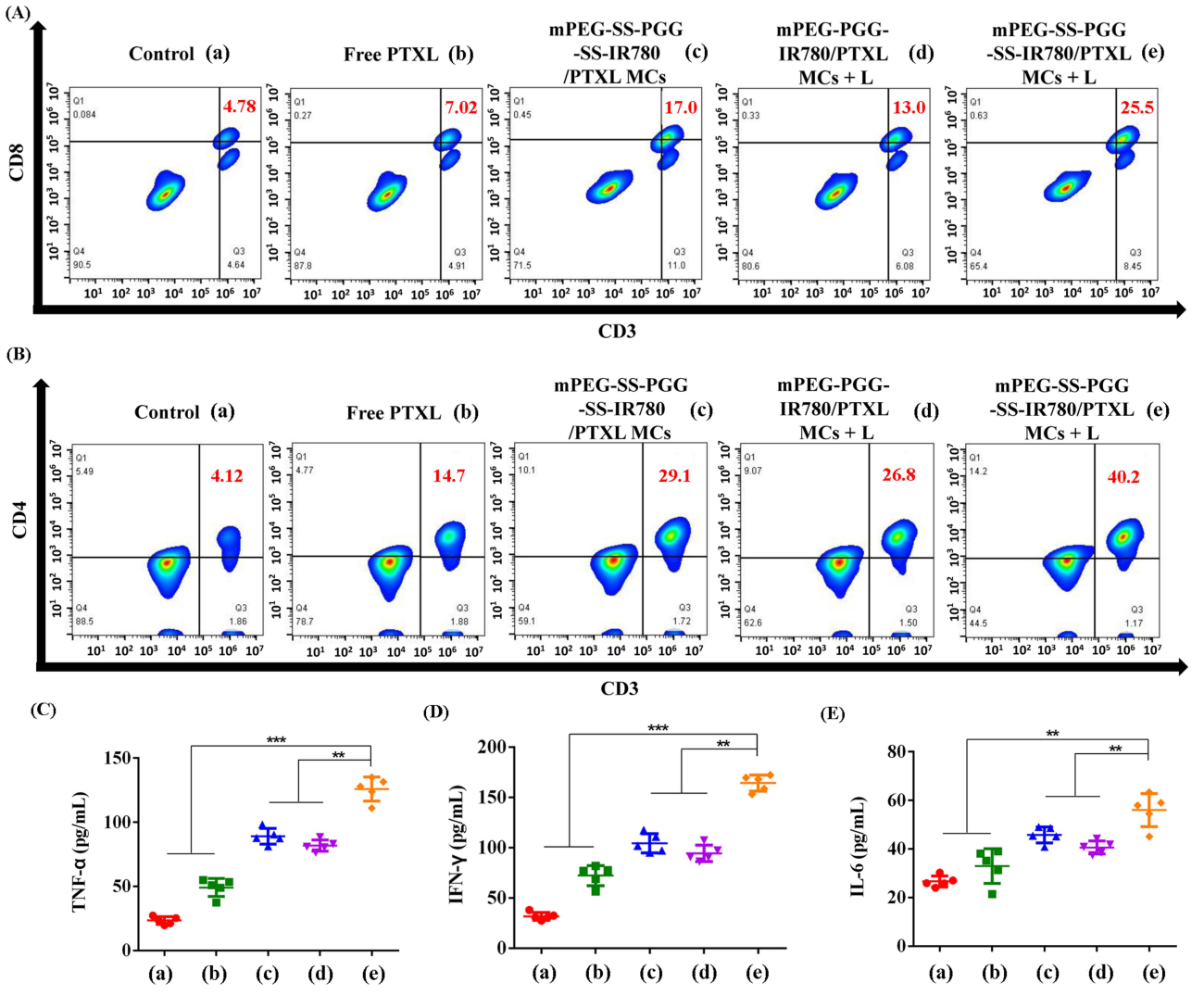

Figure 10 Representative FCM profiles of $CD3^+CD8^+$ T cells (**A**) and $CD3^+CD4^+$ T cells (**B**) in tumor. ELISA analysis of intraserous cytokine levels of TNF-α (**C**), IFN-γ (**D**), and IL-6 (**E**) after different treatments on day 21 (n = 5, $^{**}P < 0.01$, $^{***}P < 0.001$).

Abbreviations: FCM, flow cytometry; ELISA, enzyme-linked immunosorbent assay; TNF, tumor necrosis factor; IFN, interferon; IL, interleukins.

the dual stimuli sensitivity, mitochondrial targeting, PTT/PDT/CT combination therapy, and ICD, proving that mPEG-SS-PGG-SS-IR780/PTXL MCs could enable improve the antitumor efficacy to reach full potential. In addition, the results of relative body weight changes (Figure 9D), blood biochemistry tests (AST, ALT, Cr, and BUN; Figures 9E and F), blood routine tests (WBC, RBC, PLT, and HGB; Figure 9G), and H&E assays (Figure 9H) confirmed that mPEG-SS-PGG-SS-IR780/PTXL MCs possessed good biosafety under laser irradiation in-vivo.

Intra-tumoral effector T cells were detected by FCM to verify the role of mPEG-SS-PGG-SS-IR780/PTXL MCs in improving T cell-mediated antitumor immune responses. The mPEG-SS-PGG-SS-IR780/PTXL MCs + L group showed the strongest $CD8^+$ and $CD4^+$ effector T cell infiltration and the highest cytotoxic T cell and helper T cell ratios (Figures 10A and B). Moreover, the intraserous cytokine levels of TNF-α, IFN-γ, and IL-6 in serum was detected using ELISA kits. The serum levels of TNF-α, IFN-γ, and IL-6, which have antitumor immunomodulatory effects, significantly increased in mice treated with the mPEG-SS-PGG-SS-IR780/PTXL MCs + L group (Figures 10C–E). Overall, these results illustrated that the mPEG-SS-PGG-SS-IR780/PTXL MCs could induce the potent ICD of cancer cells, which, in turn, improved the systemic antitumor immunity.

Conclusion

Dual stimuli-responsive micelles were developed for imaging-guided mitochondrion-targeted PTT/PDT/CT combination therapy to induce ICD. The amphiphilic polymer mPEG-SS-PGG-SS-IR780 was synthesized by grafting IR780 with biodegradable PGG as the main chain, and mPEG-SS-PGG-SS-IR780/PTXL MCs was synthesized by loading PTXL inside the hydrophobic core. The three-mode combination nano-therapeutic system was effective to inhibit tumor growth and enhance the therapeutic efficacy of immunotherapy in-vitro and -vivo. Moreover, mPEG-SS-PGG-SS-IR780/PTXL MCs could be therapeutic and diagnostic via imaging capabilities. In summary, the mPEG-SS-PGG-SS-IR780/PTXL MCs delivery system has great potential in targeting tumor ICD combined treatment.

Acknowledgments

This work was financially supported by the Natural Science Fund of Shandong Province (No. ZR2019PH061, ZR2022LSW002, ZR2020KH015), the National Natural Science Foundation of China (No. 82002604, 81772281), the Shandong Province Taishan Scholar Project (No. ts201712067), the Support Plan for Youth Entrepreneurship and Technology of Colleges and Universities in Shandong (grant no. 2021KJ101), and Home for Researchers (www.home-for-researchers.com).

Disclosure

The authors report no conflicts of interest in this work.

References

1. Huang Z, Wang Y, Yao D, et al. Nanoscale coordination polymers induce immunogenic cell death by amplifying radiation therapy mediated oxidative stress. *Nat Commun*. 2021;12(1):145–163. doi:10.1038/s41467-020-20243-8
2. Wu H, Du X, Xu J, et al. Multifunctional biomimetic nanoplatform based on photodynamic therapy and DNA repair intervention for the synergistic treatment of breast cancer. *Acta Biomaterialia*. 2022;S1742-7061(22):00813. doi:10.1016/j.actbio.2022.12.010
3. Ding M, Zhang Y, Yu N, et al. Augmenting immunogenic cell death and alleviating myeloid-derived suppressor cells by sono-activatable semiconducting polymer nanopartners for immunotherapy. *Adv Mater*. 2023:e2302508. doi:10.1002/adma.202302508
4. Oresta B, Pozzi C, Braga D, et al. Mitochondrial metabolic reprogramming controls the induction of immunogenic cell death and efficacy of chemotherapy in bladder cancer. *Sci Transl Med*. 2021;13(575):eaba6110. doi:10.1126/scitranslmed.aba6110
5. Wan J, Zhang X, Li Z, et al. Oxidative stress amplifiers as immunogenic cell death nanoinducers disrupting mitochondrial redox homeostasis for cancer immunotherapy. *Adv Healthcare Mater*. 2022:e2202710. doi:10.1002/adhm.202202710
6. Kroemer G, Galassi C, Zitvogel L, et al. Immunogenic cell stress and death. *Nat Immunol*. 2022;23(4):487–500. doi:10.1038/s41590-022-01132-2
7. Alzeibak R, Mishchenko TA, Shilyagina NY, et al. Targeting immunogenic cancer cell death by photodynamic therapy: past, present and future. *J Immunother Cancer*. 2021;9(1):e001926. doi:10.1136/jitc-2020-001926
8. Jiang H, Fu H, Guo Y, et al. Evoking tumor associated macrophages by mitochondria-targeted magnetothermal immunogenic cell death for cancer immunotherapy. *Biomaterials*. 2022;289:121799. doi:10.1016/j.biomaterials.2022.121799
9. Wei B, Pan J, Yuan R, et al. Polarization of tumor-associated macrophages by nanoparticle-loaded Escherichia coli combined with immunogenic cell death for cancer immunotherapy. *Nano Lett*. 2021;21(10):4231–4240. doi:10.1021/acs.nanolett.1c00209
10. Jiang M, Zeng J, Zhao L, et al. Chemotherapeutic drug-induced immunogenic cell death for nanomedicine-based cancer chemo-immunotherapy. *Nanoscale*. 2021;13(41):17218–17235. doi:10.1039/d1nr05512g
11. Kou Q, Huang Y, Su Y, et al. Erythrocyte membrane-camouflaged DNA-functionalized upconversion nanoparticles for tumor-targeted chemotherapy and immunotherapy. *Nanoscale*. 2023. doi:10.1039/d3nr00542a

12. Widjaya A, Liu Y, Yang Y, et al. Tumor-permeable smart liposomes by modulating the tumor microenvironment to improve the chemotherapy. *J Controlled Release*. 2022;344:62–79. doi:10.1016/j.jconrel.2022.02.020
13. Ma B, Sheng J, Wang P, et al. Combinational phototherapy and hypoxia-activated chemotherapy favoring antitumor immune responses. *Int J Nanomedicine*. 2019;14:4541–4558. doi:10.2147/IJN.S203383
14. Li Z, Lai X, Fu S, et al. Immunogenic cell death activates the tumor immune microenvironment to boost the immunotherapy efficiency. *Adv Sci*. 2022;9(22):e2201734. doi:10.1002/advs.202201734
15. Mai Z, Zhong J, Zhang J, et al. Carrier-free immunotherapeutic nano-booster with dual synergistic effects based on glutaminase inhibition combined with photodynamic therapy. *ACS nano*. 2023. doi:10.1021/acsnano.2c11037
16. Xu M, Zhang C, He S, et al. Activatable immunoprotease nanorestimulator for second near-infrared photothermal immunotherapy of cancer. *ACS Nano*. 2023;17(9):8183–8194. doi:10.1021/acsnano.2c12066
17. Wang L, Niu C. IR780-based nanomaterials for cancer imaging and therapy. *J Mater Chem B*. 2021;9(20):4079–4097. doi:10.1039/d1tb00407g
18. Tian H, Zhou L, Wang Y, et al. A targeted nanomodulator capable of manipulating tumor microenvironment against metastasis. *J Controlled Release*. 2022;348:590–600. doi:10.1016/j.jconrel.2022.06.022
19. Mai X, Zhang Y, Fan H, et al. Integration of immunogenic activation and immunosuppressive reversion using mitochondrial-respiration-inhibited platelet-mimicking nanoparticles. *Biomaterials*. 2020;232:119699. doi:10.1016/j.biomaterials.2019.119699
20. Li Z, Chu Z, Yang J, et al. Immunogenic cell death augmented by manganese zinc sulfide nanoparticles for metastatic melanoma immunotherapy. *ACS nano*. 2022;16(9):15471–15483. doi:10.1021/acsnano.2c08013
21. Yan J, Wang C, Jiang X, et al. Application of phototherapeutic-based nanoparticles in colorectal cancer. *Int J Biol Sci*. 2021;17(5):1361–1381. doi:10.7150/ijbs.58773
22. Maggi F, Manfredi A, Carosio F, et al. Toughening polyamidoamine hydrogels through covalent grafting of short silk fibers. *Molecules*. 2022;27 (22). doi:10.3390/molecules27227808
23. Li Y, Zhang T, Liu Q, et al. PEG-derivatized dual-functional nanomicelles for improved cancer therapy. *Front Pharmacol*. 2019;10:808–822. doi:10.3389/fphar.2019.00808
24. Fujiwara Y, Mukai H, Saeki T, et al. A multi-national, randomised, open-label, parallel, phase III non-inferiority study comparing NK105 and paclitaxel in metastatic or recurrent breast cancer patients. *Br J Cancer*. 2019;120(5):475–480. doi:10.1038/s41416-019-0391-z
25. Yang D, Liu X, Jiang X, et al. Effect of molecular weight of PGG-paclitaxel conjugates on *in vitro* and *in vivo* efficacy. *J Controlled Release*. 2012;161(1):124–131. doi:10.1016/j.jconrel.2012.04.010
26. Yang D, Van S, Liu J, et al. Physicochemical properties and biocompatibility of a polymer-paclitaxel conjugate for cancer treatment. *Int J Nanomedicine*. 2011;6:2557–2566. doi:10.2147/IJN.S25044
27. Yu J, Sun L, Zhou J, et al. Self-assembled tumor-penetrating peptide-modified poly(l-gamma-glutamylglutamine)-paclitaxel nanoparticles based on hydrophobic interaction for the treatment of glioblastoma. *Bioconjug Chem*. 2017;28(11):2823–2831. doi:10.1021/acs.bioconjchem.7b00519
28. Peng L, Yu L, Howell S, et al. Effects of solution concentration on the physicochemical properties of a polymeric anticancer therapeutic. *Mol Pharm*. 2012;9(1):37–47. doi:10.1021/mp2002208
29. Saleh T, Soudi T, Shojaosadati S. Redox responsive curcumin-loaded human serum albumin nanoparticles: preparation, characterization and *in vitro* evaluation. *Int J Biol Macromol*. 2018;114:759–766. doi:10.1016/j.ijbiomac.2018.03.085
30. Mahdavi Firouzabadi B, Gigliobianco MR, Joseph JM, et al. Design of nanoparticles in cancer therapy based on tumor microenvironment properties. *Pharmaceutics*. 2022;14(12):2708–2747. doi:10.3390/pharmaceutics14122708
31. Zhang P, Cui Y, Wang J, et al. Dual-stimuli responsive smart nanoprobe for precise diagnosis and synergistic multi-modalities therapy of superficial squamous cell carcinoma. *J Nanobiotechnology*. 2023;21(1):4–23. doi:10.1186/s12951-022-01759-1
32. Ruan S, Yin W, Chang J, et al. Acidic and hypoxic tumor microenvironment regulation by CaO_2-loaded polydopamine nanoparticles. *J Nanobiotechnology*. 2022;20(1):544–558. doi:10.1186/s12951-022-01752-8
33. Huang S, Yeh N, Wang T, et al. Onion-like doxorubicin-carrying polymeric nanomicelles with tumor acidity-sensitive dePEGylation to expose positively-charged chitosan shell for enhanced cancer chemotherapy. *Int J Biol Macromol*. 2022;227:925–937. doi:10.1016/j.ijbiomac.2022.12.172
34. Zhang T, Hou X, Kong Y, et al. A hypoxia-responsive supramolecular formulation for imaging-guided photothermal therapy. *Theranostics*. 2022;12 (1):396–409. doi:10.7150/thno.67036
35. Zhang T, Wu B, Akakuru O, et al. Hsp90 inhibitor-loaded IR780 micelles for mitochondria-targeted mild-temperature photothermal therapy in xenograft models of human breast cancer. *Cancer Lett*. 2021;500:41–50. doi:10.1016/j.canlet.2020.12.028
36. Machado MGC, de Oliveira MA, Lanna EG, et al. Photodynamic therapy with the dual-mode association of IR780 to PEG-PLA nanocapsules and the effects on human breast cancer cells. *Biomed Pharm*. 2022;145:112464. doi:10.1016/j.biopha.2021.112464
37. Kim S, Choi Y, Kim K. Coacervate-mediated novel pancreatic cancer drug aleuria aurantia lectin delivery for augmented anticancer therapy. *Biomaterials Res*. 2022;26(1):35–47. doi:10.1186/s40824-022-00282-6
38. Zhang L, Sun J, Huang W, et al. Hypoxia-triggered bioreduction of poly(N-oxide)-drug conjugates enhances tumor penetration and antitumor efficacy. *J Am Chem Soc*. 2023. doi:10.1021/jacs.2c10188
39. Cheng X, Wang L, Liu L, et al. A sequentially responsive cascade nanoplatform for increasing chemo-chemodynamic therapy. *Colloids Surf B Biointerfaces*. 2022;222:113099. doi:10.1016/j.colsurfb.2022.113099
40. Liang Y, Wang P, Li Y, et al. Multistage O_2-producing liposome for MRI-guided synergistic chemodynamic/chemotherapy to reverse cancer multidrug resistance. *Int J Pharm*. 2022;631:122488. doi:10.1016/j.ijpharm.2022.122488
41. Kadkhoda J, Tarighatnia A, Nader N, et al. Targeting mitochondria in cancer therapy: insight into photodynamic and photothermal therapies. *Life Sci*. 2022;307:120898. doi:10.1016/j.lfs.2022.120898
42. Ding Y, Han J, Tian B, et al. Hepatoma-targeting and pH-sensitive nanocarriers based on a novel D-galactopyranose copolymer for efficient drug delivery. *Int J Pharm*. 2014;477(1–2):187–196. doi:10.1016/j.ijpharm.2014.10.024
43. Jiang D, Gao T, Liang S, et al. Lymph node delivery strategy enables the activation of cytotoxic T lymphocytes and natural killer cells to augment cancer immunotherapy. *ACS Appl Mater Interfaces*. 2021;13(19):22213–22224. doi:10.1021/acsami.1c03709
44. Hu J, Liang M, Ye M, et al. Reduction-triggered polycyclodextrin supramolecular nanocage induces immunogenic cell death for improved chemotherapy. *Carbohydr Polym*. 2023;301(Pt B):120365. doi:10.1016/j.carbpol.2022.120365

45. Yang S, Wu G, Li N, et al. A mitochondria-targeted molecular phototheranostic platform for NIR-II imaging-guided synergistic photothermal/photodynamic/immune therapy. *J Nanobiotechnology*. 2022;20(1):475–492. doi:10.1186/s12951-022-01679-0
46. Gao M, Huang X, Wu Z, et al. Synthesis of a versatile mitochondria-targeting small molecule for cancer near-infrared fluorescent imaging and radio/photodynamic/photothermal synergistic therapies. *Mater Today Bio*. 2022;15:100316. doi:10.1016/j.mtbio.2022.100316